

How swimming style and schooling affect the hydrodynamics of two accelerating wavy hydrofoils

Zhonglu Lin ^{a,b}, Amneet Pal Singh Bhalla ^c, Boyce E. Griffith ^d, Zi Sheng ^{a,e}, Hongquan Li ^a, Dongfang Liang ^b, Yu Zhang ^{a,*}

^a Key Laboratory of Underwater Acoustic Communication and Marine Information Technology of the Ministry of Education, College of Ocean and Earth Sciences, Xiamen University, China

^b Engineering Department, University of Cambridge, United Kingdom

^c Department of Mechanical Engineering, San Diego State University, United States

^d Departments of Mathematics and Biomedical Engineering and Carolina Center for Interdisciplinary Applied Mathematics, University of North Carolina at Chapel Hill, United States

^e Key Laboratory of Underwater Acoustic Communication and Marine Information Technology of the Ministry of Education, School of Informatics, Xiamen University, China

ARTICLE INFO

MSC:

76Z10

17-08

76M25

Keywords:

Fish swimming

Fish schooling

Fluid–structure interaction

Computational fluid dynamics

Immersed boundary method

Numerical simulation

ABSTRACT

Fish schools can make frequent accelerations that are almost simultaneous. While schooling at constant speed is well studied, far less is known concerning accelerating fish school across various body caudal fin swimming styles. The present study investigates the effects of swimming styles and schooling on two accelerating wavy hydrofoils in a free stream flow at wavelengths $\lambda = 0.5 - 8$, Strouhal number $St = 0.2 - 0.7$, front–back distance $D = 0, 0.25, 0.5, 0.75$, phase difference $\phi/\pi = 0, 0.5, 1, 1.5$, and lateral gap distance $G = 0.25, 0.3, 0.35$ with fixed Reynolds number $Re = 5000$ and maximum amplitude $A_{max} = 0.1$. In total, 591 cases were simulated using open-source software IBAMR based on immersed boundary method. Low and high wavelengths correspond to advantageous propulsive efficiency and thrust, respectively. The highest group propulsive efficiency is obtained at low wavelength $\lambda < 1.2$. At a side-by-side arrangement, the thrust upon the two foils can be equivalent across various wavelengths, indicating a synchronised acceleration. At staggered arrangement, the follower can take significant advantage of the leader in locomotion performance by tuning phase difference, especially at high wavelengths and close distances. Front–back distance is a key factor affecting the follower's propulsive efficiency for short-wavelength swimmers, but not for long-wavelength ones. Various combinations of wavelength and relative distance can lead to distinct flow structures, indicating a tunable stealth capacity of the accelerating fish schools.

1. Introduction

Drawing inspiration from nature has been proven an effective way to resolve engineering problems, referred to as “biomimetics” (Bhushan, 2009). Due to potential biomimetic applications on robotic fish (Fish, 2020), fish swimming has attracted extensive research (Triantafyllou et al., 2000; Liao, 2007) in many aspects, including schooling (Ashraf et al., 2017), swimming styles (Webb, 1984; Borazjani and Sotiropoulos, 2010), muscle anatomy (Altringham and Ellerby, 1999), and physiology (Hunt von Herbing, 2002). Among them, swimming styles and schooling can be the two interesting elements in terms fluid–structure interaction, being helpful in designing the structure and swimming strategy for biomimetic propulsion systems (Li et al., 2020). While steady swimming fish-like locomotion in a school is relatively

well researched by biological (Ashraf et al., 2017), robotic (Li et al., 2020) and numerical (Daghooghi and Borazjani, 2015) experiments. On the other hand, far less is studied regarding linearly-accelerated fish swimming (Akanyeti et al., 2017). To our knowledge, fish school acceleration was never studied with various swimming styles.

Steady-swimming fish schooling has been extensively studied in the past decades for its hydrodynamic characteristics (Weihs, 1973, 1975; Daghooghi and Borazjani, 2015; Li et al., 2019; Godoy-Diana et al., 2019; Li et al., 2020, 2021; Gupta et al., 2021). Cross sections of two schooling fish can be represented by two vibrating cylinders immersed in quasi-static fluid; it has been identified by theoretical (Lamb, 1932; Nair and Kanso, 2007) and numerical (Gazzola et al., 2012; Lin et al., 2018b,a, 2019) methods that non-dimensional parameters such

* Corresponding author at: .

E-mail address: yuzhang@xmu.edu.cn (Y. Zhang).

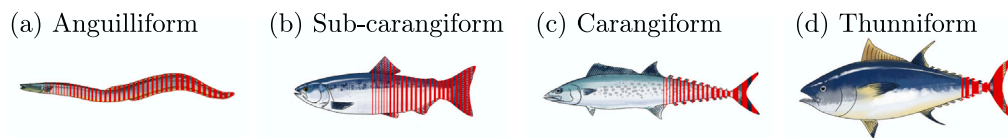


Fig. 1. Four different swimming modes of Body-Caudal-Fin type locomotion (a) Anguilliform (body undulation, e.g. eel) (b) Sub-carangiform (body undulation with caudal fin pitching, e.g. salmonid) (c) Carangiform (minor body undulation with caudal fin pitching, e.g. makrell) (d) Thunniform (mainly caudal fin pitching, e.g. tuna). The shaded area demonstrates the body parts with a significant lateral motion to generate thrust (redrawn from figures by Lindsey (1978) and Sfakiotakis et al. (1999)).

as phase difference can have a distinct impact on the flow-mediated interaction between the two cylinders. Shaw (1978) estimated that at least 25% of all fish species demonstrate schooling behaviour. Many hydrodynamic studies have focused on the minimal school composed of 2 identical BCF swimmers, using robotic fish (Li et al., 2020), biological fish (Ashraf et al., 2016; Li et al., 2020), hydrofoil experiments (Dewey et al., 2014; Kurt et al., 2020) and numerical simulation (Khalid et al., 2016; Li et al., 2019). Ashraf et al. (2016) discovered a pair of red nose tetra fish tend to swim either in-phase or anti-phase, with the latter mode being more favourable; lateral and front-back distances are around 0.5 and 0.2 fish body length. For this reason, we emphasise side-by-side and anti-phase scenarios in later discussions. Li et al. (2020) found that the locomotion efficiency of the followers can be achieved at any relative leader-follower front-back distance by adjusting their tailbeat phase difference. As for the schooling size larger than 2, Ashraf et al. (2017) discovered that the phalanx, i.e. the side-by-side arrangement of multiple fish, formation is most frequently observed in the schooling of red nose tetra fish, *Hemigrammus bleheri*, which is contradictory with the previous idea that a diamond pattern is more efficient (Weihs, 1973). In the present work, we set the front-back and lateral distances in a range similar to the previous works (Ashraf et al., 2016, 2017; Li et al., 2020).

Acceleration is also vital for fish schooling (Tytell, 2004). Fish individuals in schools can be oriented towards the same direction, stably spaced with identical speed (Partridge, 1981, 1982). Schools can also make frequent accelerations that are almost simultaneous (Zheng et al., 2005; Lecheval et al., 2018). While steady swimming for a single or schooling fish is generally well researched as aforementioned, fewer studies focused on a single fish performing C-start (Eaton et al., 1977; Tytell and Lauder, 2008; Borazjani et al., 2012; Borazjani, 2013) or linear acceleration (Tytell, 2004; Akanyeti et al., 2017; Wen et al., 2018), and even fewer for accelerating fish schools (Webb, 1983; Deng and ming Shao, 2006). Tytell (2004) and Wise et al. (2018) studied the linear acceleration from a non-zero velocity by an eel and a sunfish, respectively. Deng and ming Shao (2006) simulated a diamond-shaped fish school at constant speed and acceleration. Akanyeti et al. (2017) experimentally studied the propulsive efficiency of a single robotic fish accelerating (or decelerating), revealing the distinct hydrodynamic mechanism of vortex ring modulation. The definition of propulsive efficiency in the present paper is consistent with that used by Akanyeti et al. (2017); we will elaborate on this definition in Section 2 Methodology. The experiment by Akanyeti et al. (2017) utilised a tethered undulating fish-like model with non-zero net thrust, which is very similar to the problem setup of the present study. Based on the discovery regarding the single accelerating fish, it is reasonable to postulate that an accelerating fish school may also contain special mechanisms.

Fish swimming style is a curious topic that has fascinated many researchers (Sfakiotakis et al., 1999; Borazjani and Sotiropoulos, 2008, 2009, 2010; Tytell et al., 2010; Cui et al., 2018; Thekkethil et al., 2017, 2018, 2020). Sfakiotakis et al. (1999) categorised fish swimming styles into several classes, among which the most common one is the body-caudal fin (BCF) swimming style (Webb, 1984), featuring the body/tail undulation as the main propulsion generator. More than 88% of fish species undulate in BCF modes for propulsion (Videler, 1993; Borazjani and Sotiropoulos, 2008, 2009). BCF styles can be further divided into four types: anguilliform, sub-carangiform, carangiform, and thunniform, as exemplified in Fig. 1. Anguilliform swimmers usually undulate

in short wavelength and swim at lower velocity, whereas thunniform swimmers are mainly driven by the pitching of the posterior part and swim at higher velocity. Borazjani and Sotiropoulos (2008, 2009, 2010) conducted a series of studies on anguilliform and thunniform swimmers via high-fidelity 3D simulations. Thekkethil et al. (2017, 2018, 2020) studied undulating NACA0012 hydrofoil in various wavelengths, producing results consistent with fish in nature. They represented different swimming styles by non-dimensional wavelength $\lambda = \lambda'/C$, where λ' is the swimming undulation wavelength and C is the fish chord length. For example, anguilliform is typically represented by low wavelength $\lambda < 1$, whereas the characteristics of thunniform swimming can be captured by high wavelength $\lambda \gg 1$. Thekkethil et al. (2018) discovered that low wavelength λ swimmers generate thrust by the pressure difference between anterior and posterior body parts, whereas high λ transfer streamwise momentum by pendulum-like motion; small λ , e.g. anguilliform swimmers, generally causes high locomotion efficiency but low thrust production, and vice versa for large λ , e.g. thunniform swimmers. The numerical results obtained by Thekkethil et al. (2018) are highly coherent with previously reported single-fish swimming characteristics (Borazjani and Sotiropoulos, 2008, 2009). The present study adopts the same simplified geometry and kinematic formula proposed by Thekkethil et al. (2018), which will be presented later.

In addition, from the biological perspective, the schooling phenomenon is reported for swimmers of sub-carangiform (Trevorrow, 1998), carangiform (Axelsen et al., 2001; Guillard et al., 2006; Hemelrijk et al., 2010) and thunniform (Dai et al., 2020; Mitsunaga et al., 2013; Uranga et al., 2019); anguilliform species seem never found to exhibit schooling behaviour in the wild, although European eels were reported to produce better efficiency while schooling in the laboratory (Burgerhout et al., 2013). Although hydrodynamics may not be the only factor affecting fish's schooling tendency, based on this natural observation, it is not unreasonable to hypothesise that high wavelength propellers are more suited for schooling than low wavelength ones.

In summary, for BCF swimmers, the mechanism of *constant-speed schooling* has been extensively studied (Weihs, 1973, 1975; Daghooghi and Borazjani, 2015; Ashraf et al., 2016; Li et al., 2020), yet relatively scarce is the research on accelerating *schooling* swimmers with various *swimming styles*. This paper studies the hydrodynamics of two accelerating wavy hydrofoils with various swimming styles interacting in free-stream flow. The present study help to design future underwater propellers, which may involve multiple wavy hydrofoils with variable swimming styles or wavelengths. This work is a continuation of the previous single swimmer acceleration study conducted by Akanyeti et al. (2017) and Thekkethil et al. (2018) and has been inspired by the previous 3D numerical (Borazjani and Sotiropoulos, 2010), biological (Ashraf et al., 2017) and robotic (Li et al., 2020) fish schooling studies in the steady swimming condition.

2. Methodology

This section describes the numerical methodology for studying the fish schooling and swimming styles' combined effects on propulsive hydrodynamics. This problem is represented by two identical wavy hydrofoils tethered in a free-stream flow, as presented in Section 2.1. Numerical simulation is then executed by IBAMR (Griffith, 2013), an extensively-validated immersed boundary software, as discussed in

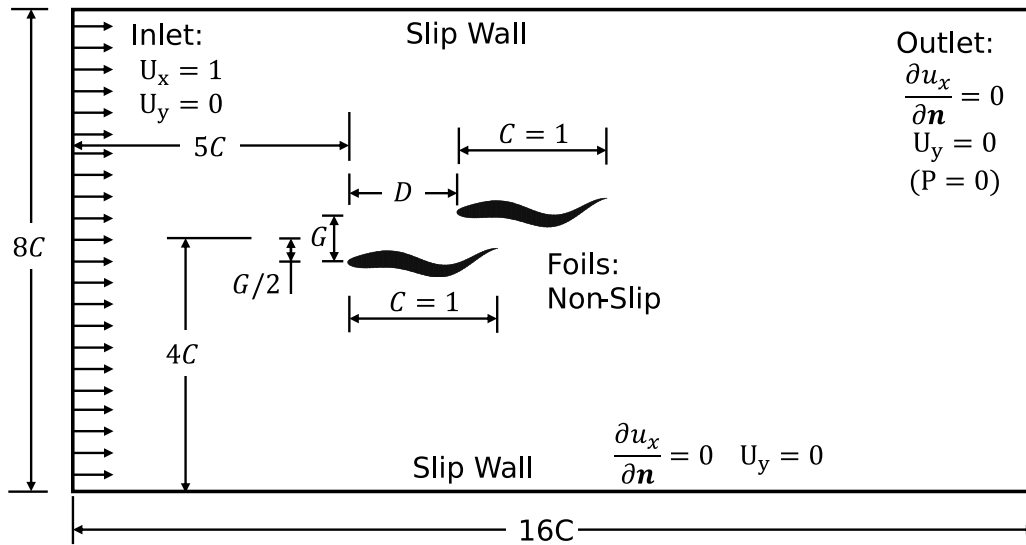


Fig. 2. Problem setup of this two fish case.

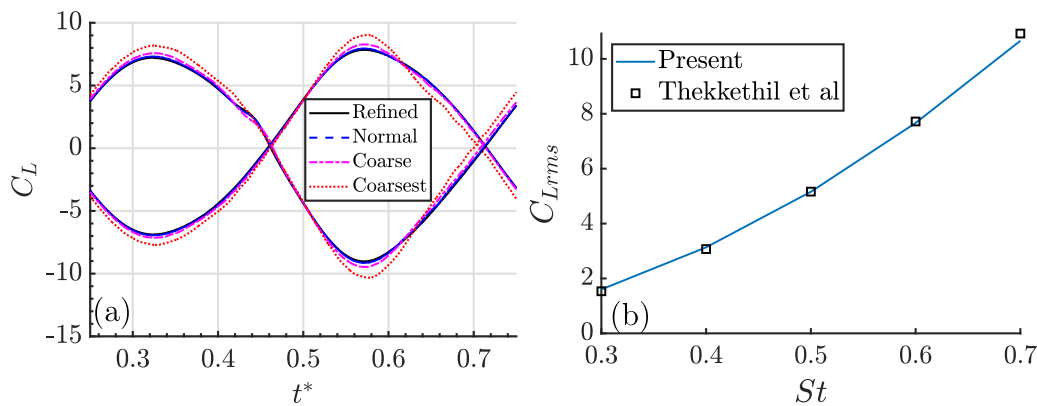


Fig. 3. (a) Mesh independence study for meshes listed in Table 3 with $Re = 5000$, $St = 0.4$, $A_{max} = 0.1$, $\lambda = 2$, $\phi/\pi = 1$, $G = 0.3$, $D = 0.5$. (b) Validation by comparing present results with that from Thekkethil et al. (2018, pp. 10) with $Re = 5000$, $St = 0.3 - 0.7$, $A_{max} = 0.1$, $\lambda = 1.5$.

Section 2.2. The kinematic model of hydrofoil undulation is formulated by the classic travelling wave equation with additional consideration upon the wavelengths as shown in Section 2.3. Dimensional analysis is conducted in Section 2.4 to formalise the investigated problem. Mesh convergence study and validation can be found in Section 2.5.

2.1. Physical problem setup

In this paper, the two undulating rigid NACA0012 hydrofoils are fixed at their initial locations, i.e. the foils are “tethered”. This tethered configuration to study linearly accelerating swimmers has been justified by the experimental study of Akanyeti et al. (2017), which also compared the experimental data to biological statistics. To account for the accelerating condition, the mean net thrust on the swimmers is not zero. It should be noted that the present setup differs from many previous fish schooling studies focusing on the steady swimming condition with zero net force. The non-dimensional form of the physical problem investigated in the present paper is demonstrated in Fig. 2. Here, $C = 1$ is the chord length of the two NACA0012 hydrofoils. G and D are the lateral and front-back distances between the two hydrofoils. The computational domain is $16C$ in the streamwise direction and $8C$ in the transverse direction, which is identical to the domain size chosen by Thekkethil et al. (2018). The head tip of the leader fish is placed $5C$ to the inlet. The mid-point between the two hydrofoils is placed $4C$ to each lateral wall. As for boundary conditions, the two

identical hydrofoils are both non-slip on their fluid-solid interface. The inlet free-stream velocity is configured as $U_{inlet} = (U_x, U_y) = (1, 0)$. The outlet boundary is set as $\partial u_x/\partial n = 0$ and $U_y = 0$, equivalent to the zero pressure outlet boundary condition, i.e. $P_{outlet} = 0$; here, n is the outward unit vector normal to the boundary. Lateral walls on the left and right sides of the swimming direction are prescribed as slip wall boundary conditions $\partial u_x/\partial n = 0$ and $U_y = 0$. We note that we are not strictly modelling any specific fish species but are instead seeking underlying principles of how swimming style affects accelerated schooling.

In addition, similar problem setups have been adopted and justified by robotic experiments (Akanyeti et al., 2017) and numerical simulation (Thekkethil et al., 2017, 2018, 2020; Gupta et al., 2021) to study accelerating swimmers.

2.2. Immersed boundary method

In the present study, the numerical simulation of the fluid–structure interaction process is achieved by a modified version of the constrained method in the C++ open-source software IBAMR (Griffith, 2013). IBAMR is constructed on the foundation of several libraries, including SAMRAI (Hornung and Kohn, 2002; Hornung et al., 2006), PETSc (Balay et al., 1997, 2010, 2001), hypre (Falgout et al., 2010; Balay et al., 1997), and libmesh (Kirk et al., 2006). The constrained immersed boundary (IB) method of IBAMR has been validated in

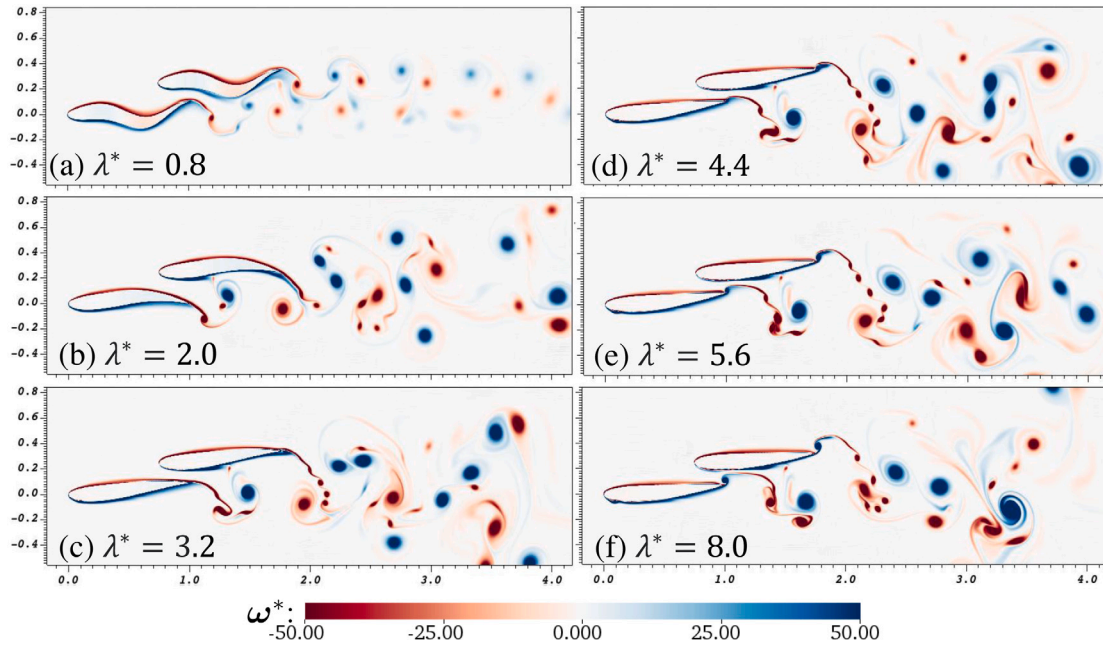


Fig. 4. Variation of hydrofoil geometry and vorticity contours at time $t^*/T = 5$ with $St = 0.4$, $G = 0.25$, $D = 0.75$, $\phi = 0$, and (a) $\lambda = 0.8$ (b) $\lambda = 2.0$ (c) $\lambda = 3.2$ (d) $\lambda = 4.4$ (e) $\lambda = 5.6$ (f) $\lambda = 8.0$. The wake structure irregularity increases with λ .

various scenarios, including fish swimming (Bhalla et al., 2013; Griffith and Patankar, 2020), flow past a cylinder (Nangia et al., 2017), and free-surface piercing (Nangia et al., 2019). In the present study, the force upon each hydrofoil was obtained by the control volume method (Nangia et al., 2017).

The IB method uses the Eulerian description for the fluid and the Lagrangian description for the deforming structure. One of its advantages is the computational efficiency of circumventing the costly remeshing process encountered in other methods like the finite element method. The implemented formulation is stated as follows:

$$\rho \left(\frac{\partial \mathbf{u}(\mathbf{x}, t)}{\partial t} + \mathbf{u}(\mathbf{x}, t) \cdot \nabla \mathbf{u}(\mathbf{x}, t) \right) = -\nabla p(\mathbf{x}, t) + \mu \nabla^2 \mathbf{u}(\mathbf{x}, t) + \mathbf{f}(\mathbf{x}, t) \quad (1)$$

$$\nabla \cdot \mathbf{u}(\mathbf{x}, t) = 0 \quad (2)$$

$$\mathbf{f}(\mathbf{x}, t) = \int_U \mathbf{F}(\mathbf{X}, t) \delta(\mathbf{x} - \chi(\mathbf{X}, t)) d\mathbf{X} \quad (3)$$

$$\frac{\partial \chi(\mathbf{X}, t)}{\partial t} = \int_{\Omega} \mathbf{u}(\mathbf{x}, t) \delta(\mathbf{x} - \chi(\mathbf{X}, t)) d\mathbf{x} \quad (4)$$

Here $\mathbf{x} = (x, y) \in \Omega$ represents fixed physical Cartesian coordinates, where Ω is the physical domain occupied by the fluid and the immersed structure. $\mathbf{X} = (X, Y) \in U$ means Lagrangian solid structure coordinates, and U is the Lagrangian coordinate domain. The mapping from Lagrangian structure coordinates to the physical domain position of point \mathbf{X} for all time t can be expressed as $\chi(\mathbf{X}, t) = (\chi_x(\mathbf{X}, t), \chi_y(\mathbf{X}, t)) \in \Omega$. In other words, $\chi(U, t) \subset \Omega$ represents the physical region occupied by the solid structure at time t . $\mathbf{u}(\mathbf{x}, t)$ is the Eulerian fluid velocity field and $p(\mathbf{x}, t)$ is the Eulerian pressure field. ρ is the fluid density. μ is the incompressible fluid dynamic viscosity. $\mathbf{f}(\mathbf{x}, t)$ and $\mathbf{F}(\mathbf{X}, t)$ are Eulerian and Lagrangian force densities, respectively. $\delta(\mathbf{x})$ is the Dirac delta function. More details regarding the constrained IB formulation and discretisation process can be found in previous literature (Bhalla et al., 2013; Griffith and Patankar, 2020).

2.3. Kinematic model for fish-like wavy propulsion

The non-dimensional kinematic equations for the centrelines of the two tethered NACA0012 hydrofoils (Langley Research Center, 2021)

are prescribed as Eqs. (5) and (6) (Thekkethil et al., 2018; Videler and Hess, 1984):

$$\Delta Y_1^* = A_{max} X_1^* \sin \left[2\pi \left(\frac{X_1^*}{\lambda} - \frac{St}{2A_{max}} t^* \right) \right] \quad (5)$$

$$\Delta Y_2^* = A_{max} X_2^* \sin \left[2\pi \left(\frac{X_2^*}{\lambda} - \frac{St}{2A_{max}} t^* \right) + \phi \right] \quad (6)$$

where $\Delta Y_i^* = \Delta Y_i/C$ is the lateral displacement of each NACA0012 hydrofoil centreline that varies with streamwise direction $X_i^* = X_i/C$ and time $t^* = tu_{\infty}/C$. The wavy undulation period T equals $2A_{max}/St$, so $t^*/T = t^*St/2A_{max}$. $i = 1$ and $i = 2$ denote the leader foil and the follower foil, respectively.

2.4. Dimensional analysis

In this paper, we investigate the flow-mediated interaction between two swimming fish with various swimming modes, which can be simplified into two rigid NACA0012 hydrofoils with wavy lateral movement subject to free stream flow. The problem setup can be determined by seven non-dimensional groups as shown in Table 1, where ρ is the fluid density, $u_{\infty} = 1$ is the free stream velocity, $C = 1$ is the hydrofoil chord length, μ is the fluid viscosity, f is the undulation frequency, a_{max} is the maximum undulation amplitude at the tail tip, λ' , g , d are the wavelength, lateral distance and front-back distance to be non-dimensionalised by chord length C . Reynolds number Re and Strouhal number St are fixed at 5000 and 0.4, respectively, since the slowly swimming fish generally swim with moderate Re and $St \approx 0.4$, $A_{max} \approx 0.1$ (Lindsey, 1978; Thekkethil et al., 2018). The Reynolds number at the order of 10^3 allows a more economical mesh resolution and computational cost, whereas predominant vortex dynamics remain understandable (Liu et al., 2017). The chosen Reynolds number is more convenient for comparison with the previous work of single wavy foil by Thekkethil et al. (2018), which also fixed Re at 5000. The lateral and front-back distances vary in the range of $G = 0.25 - 0.35$ and $D = 0 - 0.75$, respectively, which corresponds to the value range chosen by Ashraf et al. (2017) and Li et al. (2020). The wavelength varies in the range of $\lambda = 0.8 - 8.0$. The typical anguilliform swimmer of

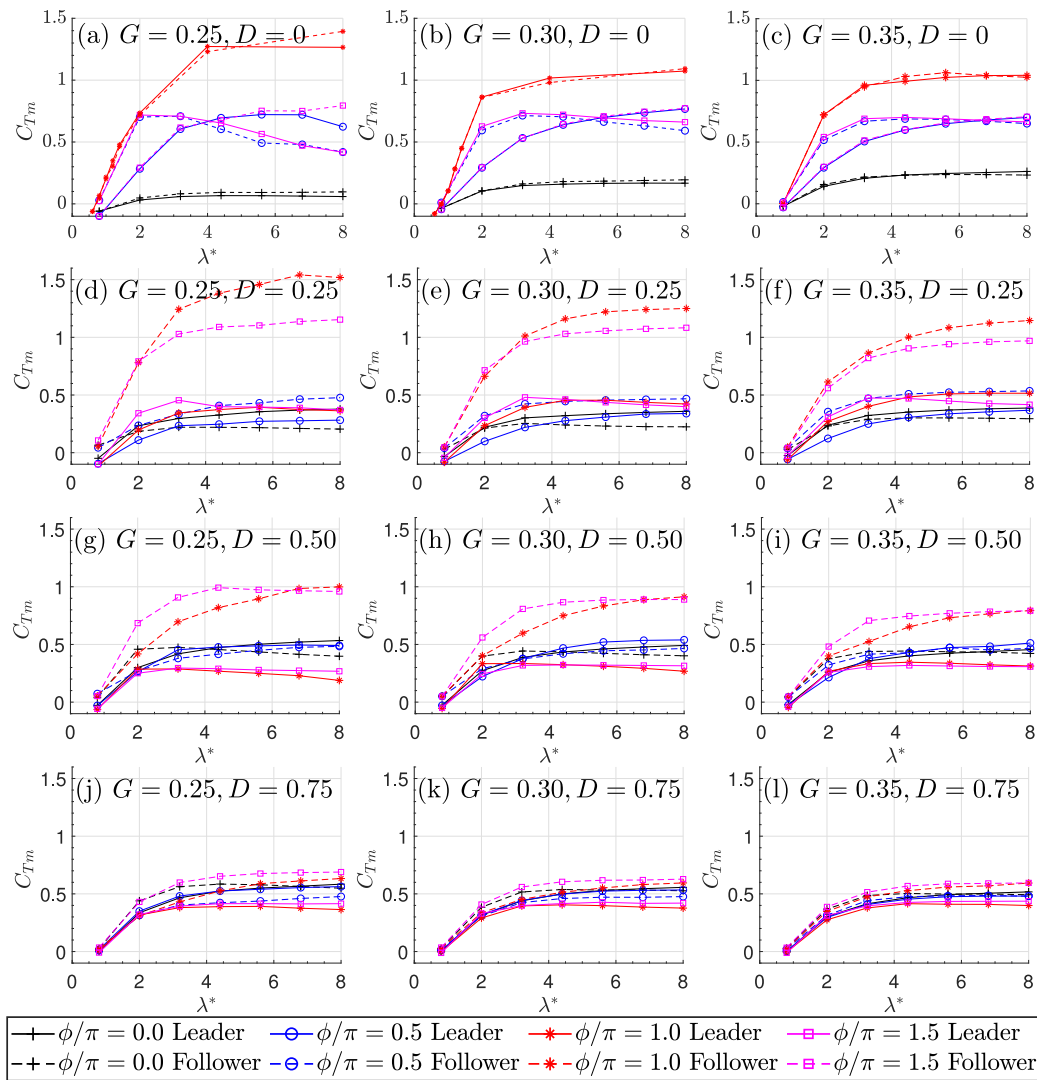


Fig. 5. Variation of mean thrust C_{Tm} for both leading swimmer (solid lines) and following swimmer (dashed lines) at Strouhal number $St = 0.4$, a series of wavelength $\lambda = 0.8-8.0$, the leader-follower phase difference $\phi/\pi = 0, 0.5, 1.0, 1.5$ (denoted by marker types), front-back distance (a-c) $D = 0.25$, (d-f) $D = 0.50$, and (g-i) $D = 0.75$; lateral gap distance at (a & d & g) $G = 0.25$, (b & e & h) $G = 0.30$, (c & f & i) $G = 0.35$.

eels undulates in the range $\lambda = 0.642 - 0.87$ (Müller et al., 2001; Borazjani and Sotiropoulos, 2009). Carangiform swimmers swim in the wavelengths $\lambda = 0.89 - 1.1$ (Borazjani and Sotiropoulos, 2008). Thunniform fish swims mainly by oscillating its almost stiff posterior part of the body (Smits, 2019), corresponding to $\lambda \gg 1$. The present parametric space also refers to a series of previous studies with a single swimmer (Liu et al., 1996; Müller et al., 1997; Nauen and Lauder, 2002; Tytell and Lauder, 2004a,b; Deng and ming Shao, 2006; Dong and Lu, 2007; Sui et al., 2007; Borazjani and Sotiropoulos, 2008, 2009; Shao et al., 2010; Thekkethil et al., 2018)

To examine the schooling performance of two fish-like hydrofoils, we chose the output parameters as listed in Table 2. Here, $F_{T,i}$ is the net thrust along the streamwise direction and $F_{L,i}$ is the lateral force in the transverse direction. $i = 1, 2$ denotes the No. i hydrofoil structure; $i = 1$ and $i = 2$ represent the leader and follower foils, respectively. $V_{body,i} = dY_i^*/dt^*$ is the lateral motion velocity of the hydrofoils. $c_{L,i}$ is the force coefficient density distributed on the surface of the hydrofoil. $\mathbf{u}(\mathbf{x}, t)$ is the velocity field of the fluid. Many previous studies focus on the steady swimming condition where the net force upon the fish is zero (Tytell and Lauder, 2004a; Borazjani and Sotiropoulos, 2008, 2009), where the Froude efficiency is defined by only the thrust without considering the drag force with equivalent magnitude, which has been proven a helpful metric. In contrast, since the present study focus on the

Table 1

Non-dimensional input parameters and the involved range of value.

| Reynolds number | Re | $\rho u_\infty C / \mu$ | 5000 |
|----------------------|-----------|-------------------------|----------------------------------|
| Strouhal number | St | $2f a_{max} / u_\infty$ | 0.2-0.7 |
| Maximum amplitude | A_{max} | a_{max} / C | 0.1 |
| Wavelength | λ | λ' / C | 0.5-8 |
| Lateral gap distance | G | g / C | 0.25, 0.3, 0.35 |
| Front-back distance | D | d / C | 0, 0.25, 0.5, 0.75 |
| Phase difference | ϕ | $\phi_2 - \phi_1$ | 0, 0.5 π , π , 1.5 π |

accelerating scenario with non-zero net force, we define the propulsive efficiency using the mean net thrust. This metric was also adopted in the previous robotic experiment (Akanyeti et al., 2017) and numerical simulations (Thekkethil et al., 2018) as a measurement of propulsive efficiency for an accelerating propeller.

2.5. Mesh independence and validation

IBAMR utilises two sets of “immersed” meshes for numerical simulations, i.e. Eulerian mesh for the flow field and Lagrangian mesh for the structure (swimmer), where the Eulerian mesh can be adaptively refined considering the local vorticity strength and adjacency to the

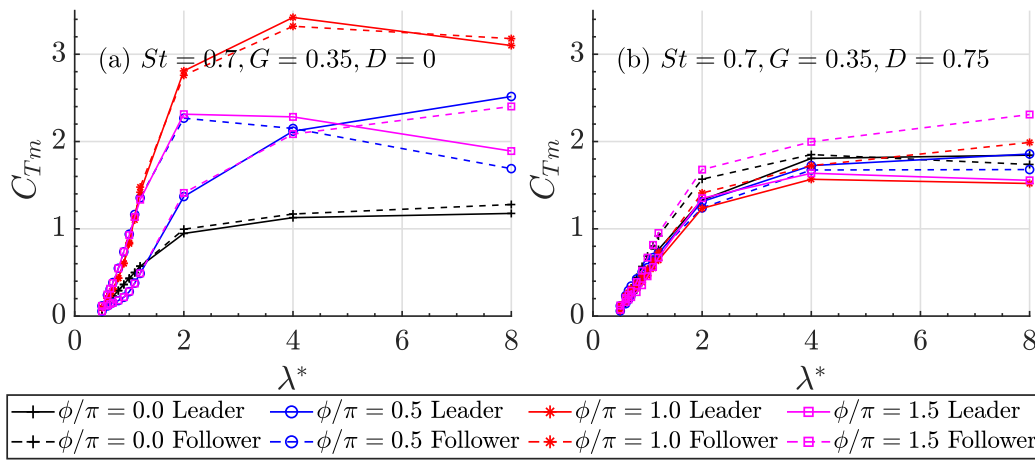


Fig. 6. Variation of mean thrust C_{Tm} for both leading swimmer (solid lines) and following swimmer (dashed lines) at Strouhal number $St = 0.7$ and lateral distance $G = 0.35$, a series of wavelength $\lambda = 0.5 - 8.0$, leader-follower phase difference $\phi/\pi = 0.0, 0.5, 1.0, 1.5$ (denoted by marker types), front-back distance (a) $D = 0$, (b) $D = 0.75$.

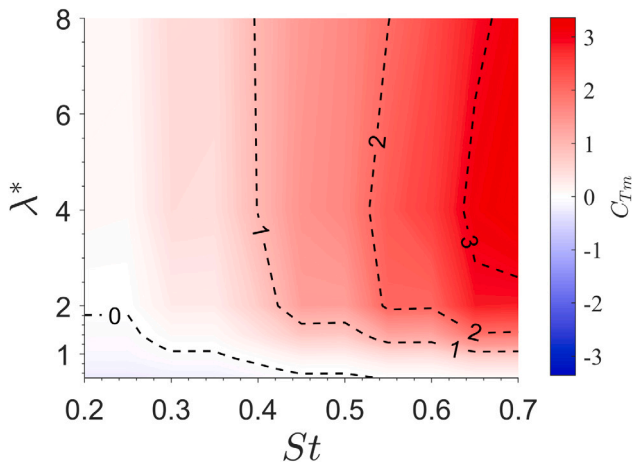


Fig. 7. The heat map denotes the propulsive force, i.e. mean net thrust C_{Tm} , as a function of Strouhal number $St = 0.2 - 0.7$ and wavelength $\lambda = 0.5 - 8$ at anti-phase $\phi/\pi = 1.0$, side-by-side formation $D = 0$, lateral gap distance at $G = 0.35$. The positive values (red) indicate conditions when the propulsive force overcomes the fluid drag, i.e. acceleration. The negative values (blue) indicate scenarios with the drag force larger than the thrust, i.e. deceleration. The contour line at $C_{Tm} = 0$ stands for cases with thrust equivalent to drag, i.e. steady swimming. High wavelength and high Strouhal number produce strong net propulsive force. (For interpretation of the references to colour in this figure legend, the reader is referred to the web version of this article.)

Table 2

Non-dimensional output parameters.

| | | |
|--|----------------|--|
| Cycle-averaged net thrust coefficient | $C_{Tm,i}$ | $\left(\frac{2F_{T,i}}{\rho u_\infty^2 C} \right)_{avg}$ |
| Root mean square lateral force coefficient | $C_{L,rms,i}$ | $\left(\frac{2F_{L,i}}{\rho u_\infty^2 C} \right)_{rms}$ |
| Propulsive efficiency (Liu et al., 1996) | η_i | $\frac{P_{out,i}}{P_{in,i}} = \frac{C_{Tm,i}}{\int c_{L,i} V_{body,i} dS}$ |
| Group propulsive efficiency | η_{group} | $\frac{\sum P_{out,i}}{\sum P_{in,i}}$ |
| Fluid velocity | u^* | u/u_∞ |
| Fluid vorticity | ω^* | $\nabla \times u^*$ |

Lagrangian described structure. In the present study, the Eulerian mesh consists of three levels of refinement divided by local vorticity thresholds, with each level being four times more refined than the coarser level. The mesh density of the Lagrangian mesh for the hydrofoil structure is equivalent to that of the most refined level Eulerian mesh for the fluid.

Table 3

Mesh configuration for independence study.

| Mesh | Refined | Normal | Coarse | Coarsest |
|-------------------------------|----------------------|--------------------|---------------------|---------------------|
| Δx_{min}^* | 2×10^{-3} | 4×10^{-3} | 8×10^{-3} | 16×10^{-3} |
| Δt^* | 2.5×10^{-5} | 5×10^{-5} | 10×10^{-5} | 20×10^{-5} |
| $\Delta x_{min}^*/\Delta t^*$ | 80 | 80 | 80 | 80 |

Mesh independence study was conducted using four meshes with different levels of refinement, as listed in Table 3. At $D = 0.5, G = 0.3, \lambda = 2.0, \phi/\pi = 1$, the time history of lateral force coefficient is examined to check mesh convergence, as seen in Fig. 3a. While a large difference can be observed from C_L yielded by the ‘‘Coarsest’’ mesh and ‘‘Coarse’’ mesh, the time history of C_L almost overlaps for the output produced by ‘‘Normal’’ and ‘‘Refined’’ meshes. To be conservative, the ‘‘Refined’’ mesh setting is chosen for all the cases in this study. Based on ‘‘Refined’’ mesh, the current result is further validated against results from Thekkethil et al. (2018, pp. 10) with the single-fish case of $Re = 5000, St = 0.3 - 0.7, A_{max} = 0.1, \lambda = 1.5$, as seen in Fig. 3b. Excellent coherence can be seen between the results produced by the present IBAMR model and the in-house model by Thekkethil et al. (2018).

3. Results and discussion

The present paper simulated 591 cases focusing on wavelengths $\lambda = 0.5 - 8.0$. The lateral gap distance G ranges from 0.25 to 0.35, the front-back distance $D = 0 - 0.75$, leader-follower phase difference $\phi/\pi = 0.0, 0.5, 1, 1.5$, the Strouhal number $St = 0.4, 0.7$. The Reynolds number and maximum amplitude are fixed at $Re = 5000$ and $A_{max} = 0.1$ throughout this study.

Several output parameters will be discussed to understand the schooling effect with various swimming styles, as listed in Table 2: the net thrust C_{Tm} is directly relevant to the acceleration of the swimming foils; propulsive efficiency η_i and η_{group} are the propulsion efficiency converting the input energy to the output locomotion performance as an individual foil and as a grouped system, respectively; vorticity distribution ω^* demonstrates the vortex interaction between the two hydrofoils and the vortex shedding pattern in the wake flow, in which the vortex interaction is significant to understand the mechanism resulting the force and efficiency distribution. In addition, the vortex wake pattern is also essential to understand the stealth capacity for fish schooling.

In the following discussion, Section 3.1 offers a quick overview of the question investigated in the present paper. Section 3.2 examines the variation of swimmers’ mean thrust with a series of non-dimensional

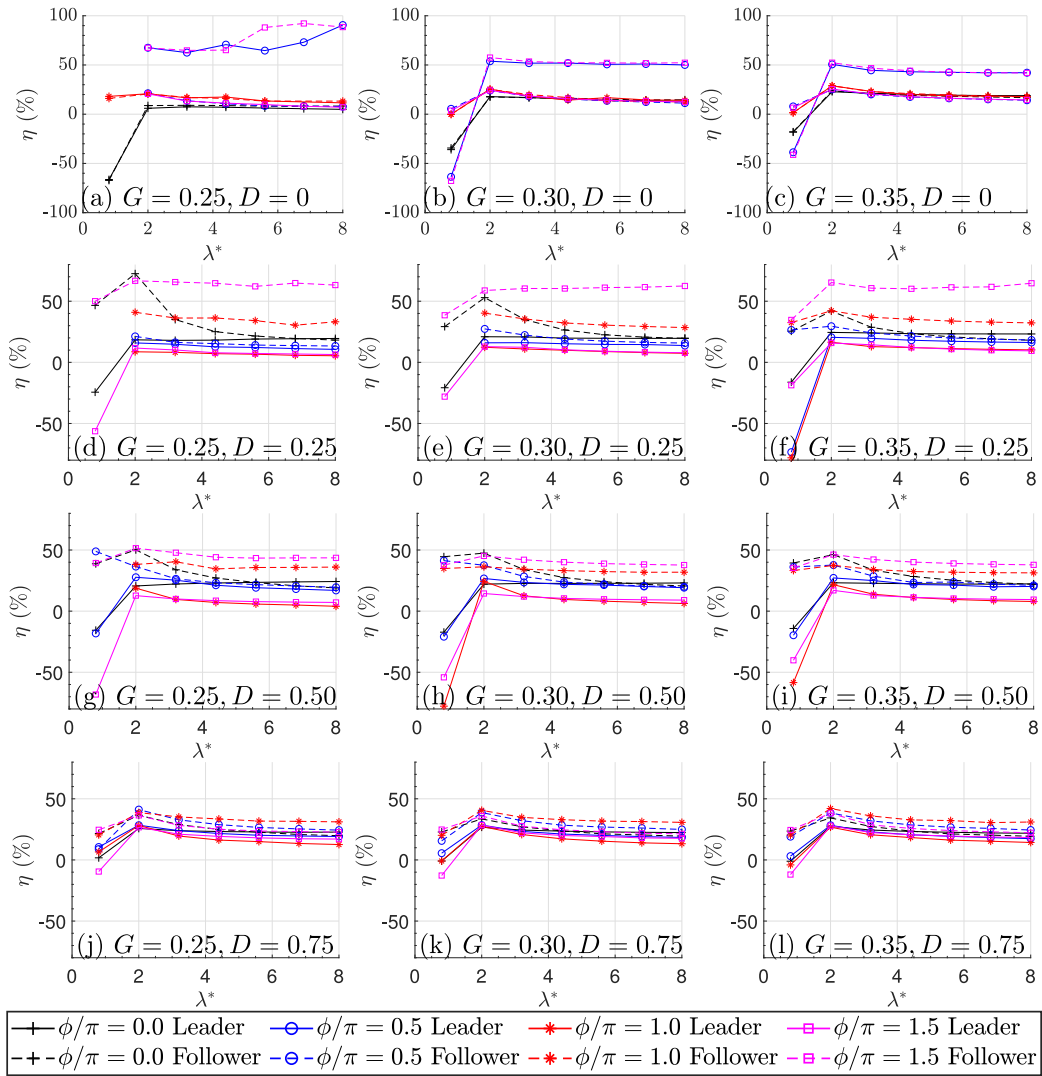


Fig. 8. Variation of propeller efficiency η for leader (solid lines) and follower (dashed lines) hydrofoils at Strouhal number $St = 0.4$, a series of wavelength $\lambda = 0.5 - 8.0$, leader-follower phase difference $\phi/\pi = 0.0, 0.5, 1.0, 1.5$ (denoted by marker types), front-back distance (a-c) $D = 0$, (d-f) $D = 0.25$, and (g-i) $D = 0.5$, (j-l) $D = 0.75$; lateral gap distance at (a & d & g & j) $G = 0.25$, (b & e & h & k) $G = 0.30$, (c & f & i & l) $G = 0.35$.

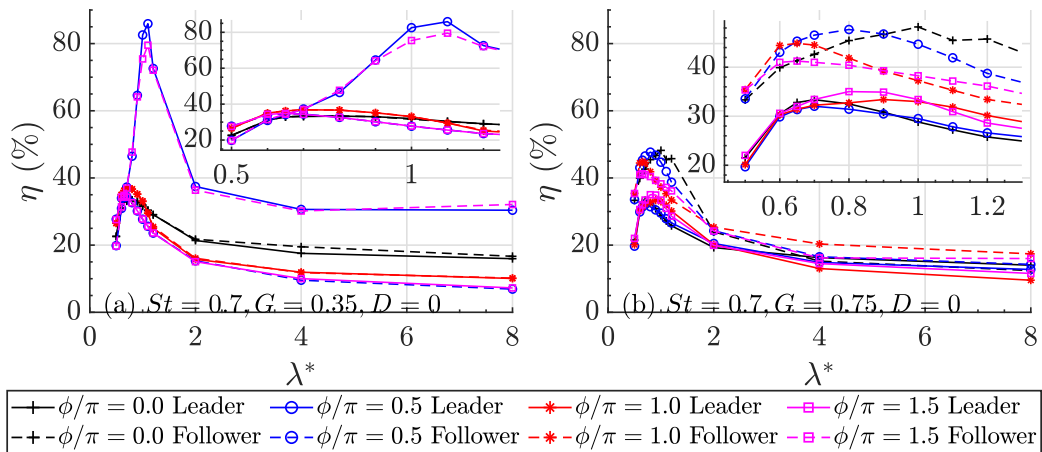


Fig. 9. Variation of propeller efficiency η for leader (solid lines) and follower (dashed lines) hydrofoils at Strouhal number $St = 0.7$, a series of wavelength $\lambda = 0.5 - 8.0$, leader-follower phase difference $\phi/\pi = 0.0, 0.5, 1.0, 1.5$ (denoted by marker types), lateral distance $G = 0.35$, and front-back distance (a) $D = 0$, (b) $D = 0.7$.

parameters focusing on the variation of wavelengths. Section 3.3 scrutinises the individual propulsive efficiency for both swimmers, whereas

Section 3.4 review the group efficiency. We discuss the flow structure at side-by-side and staggered arrangement in Sections 3.5 and 3.6

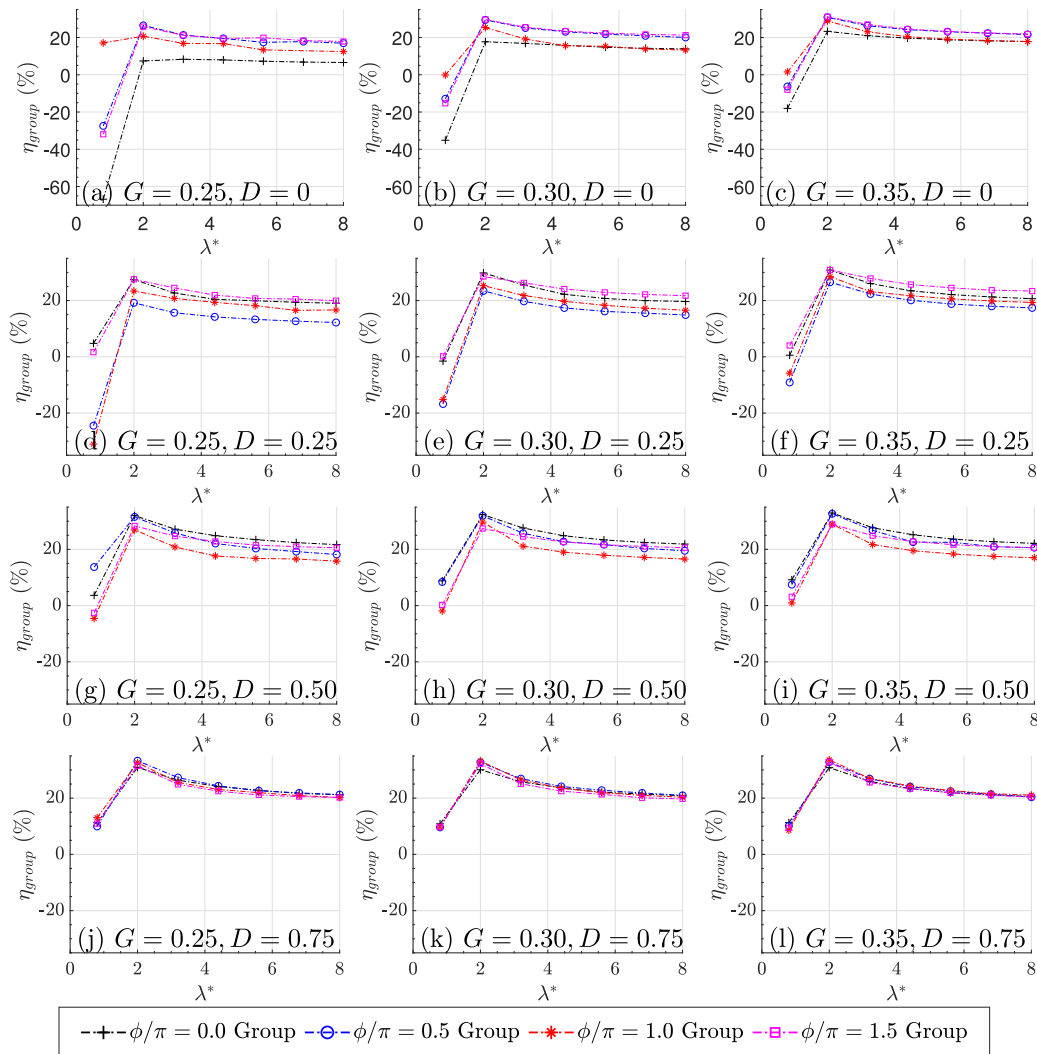


Fig. 10. Variation of group efficiency η_{group} for the swimming group at Strouhal number $St = 0.4$, a series of wavelength $\lambda = 0.8 - 8.0$, leader–follower phase difference $\phi/\pi = 0, 0.5, 1.0, 1.5$ (denoted by marker types), front–back distance (a–c) $D = 0$, (d–f) $D = 0.25$, and (g–i) $D = 0.5$, (j–l) $D = 0.75$; lateral gap distance at (a & d & g & j) $G = 0.25$, (b & e & h & k) $G = 0.30$, (c & f & i & l) $G = 0.35$.

separately due to their qualitative difference. Section 3.5 investigates the flow structure at the side-by-side arrangement with various wavelengths λ and its inter-relationships with other non-dimensional groups with the additional discussion regarding the flow symmetry and its breaking. Section 3.6 reviews the vorticity distribution at staggered formation with additional scrutinisation on the lagged vortex interaction.

3.1. Overview

In this subsection, we offer an overview of the present paper with example cases at $G = 0.25$, $D = 0.75$, $\phi = 0$ and $\lambda = 0.8 - 8.0$, as seen in Fig. 4. The irregularity of wake flow generally increases with wavelength λ , as seen in the vorticity contours in Fig. 4. The flow structure near the two foils is relatively regular. Here, we calculate output parameters using the last three relatively stable periods out of at least ten total cycles. Additional discussion regarding the time history can be found in Appendix B. Compared with single swimmer cases with similar configurations (Thekkethil et al., 2018), the interaction between two wavy foils leads to a more complicated flow structure. For convenience and conciseness, the vorticity scale in all other figures is identical to the one shown in Fig. 4.

3.2. Net thrust

This subsection discusses how swimming style/wavelengths and other non-dimensional groups affect the net thrust to accelerate the swimmers. For either the leader or the follower, mean net thrust C_{Tm} generally increases with the wavelength λ regardless of the relative distances at $G = 0.25 - 0.35$ and $D = 0 - 0.75$, as demonstrated in Fig. 5. An exception can be observed at $D = 0$ Fig. 5a and b, where the thrust peaks at $\lambda = 4.4$ while swimming in-phase or in anti-phase $\phi/\pi = 0, 1$; this could be a result of the strong vorticity and symmetry breaking at high wavelength and side-by-side configuration, which will be discussed later in Section 3.5. Maximum thrust for both swimmers is obtained at side-by-side and in-phase schooling with a high Strouhal number and high wavelength $\lambda \gg 1$ swimming style.

The qualitative difference can be observed for the effects of wavelengths λ at side-by-side $D = 0$ and staggered arrangement $D > 0$. At $D = 0$ in Fig. 5a–c, the thrust for the leader and the follower is almost equivalent across various wavelengths, while at staggered arrangement $D > 0$ in Fig. 5d–l, a large difference between the leader and the follower can be observed, especially at high wavelength $\lambda \geq 2$. At $D = 0$ in Fig. 5a–c, the variation of thrust regarding the undulation phase

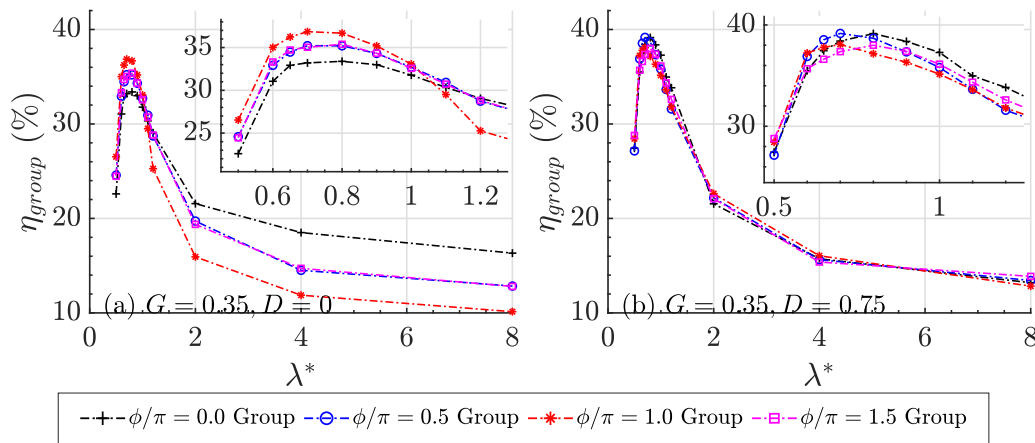


Fig. 11. Variation of group efficiency η_{group} for the swimming group at Strouhal number $St = 0.7$, lateral distance $G = 0.35$, a series of wavelength $\lambda = 0.8 - 8.0$, leader–follower phase difference $\phi/\pi = 0, 0.5, 1.0, 1.5$ (denoted by marker types), and front–back distance (a-c) $D = 0$, (d-f) $D = 0.75$.

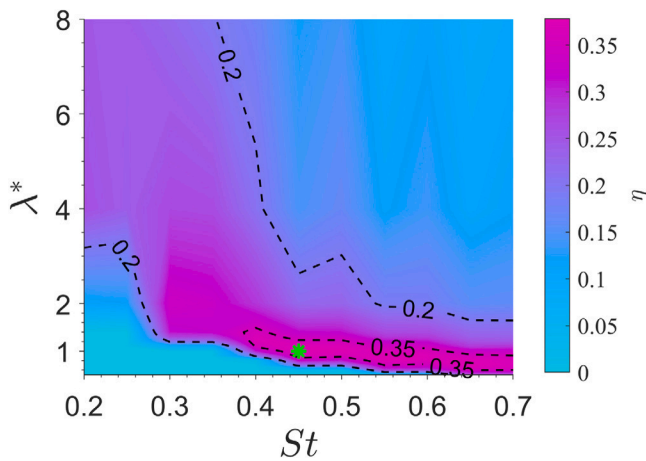


Fig. 12. The heat map denotes the propulsive efficiency $\eta_1 = \eta_2 = \eta_{group}$ as a function of Strouhal number $St = 0.2 - 0.7$ and wavelength $\lambda = 0.5 - 8$ at anti-phase $\phi/\pi = 1.0$, side-by-side formation $D = 0$, lateral gap distance at $G = 0.35$. The green star * marker denotes the location for maximum efficiency 38% at $St = 0.4$ and $\lambda = 1$. High-efficiency $\eta > 35\%$ is achieved in a narrow band with $\lambda \approx 1$, $St = 0.4 - 0.7$. At high wavelength, relatively low Strouhal number St is more efficient. For the cases with negative net thrust, $C_{Tm} < 0$, the efficiency is drawn as zero.

difference ϕ is in coherence with the observed fish schooling behaviour: when the multiple fish swim side-by-side, they tend to undulate either in-phase $\phi/\pi = 0$ or in anti-phase $\phi/\pi = 1$ (Ashraf et al., 2017).

At side-by-side arrangement $D = 0$, thrust C_{Tm} generally increases with gap distance G while swimming in-phase $\phi/\pi = 0$, but decreases with G while swimming anti-phase $\phi/\pi = 1$. As the two foils swim in-phase $\phi/\pi = 0$ and anti-phase $\phi/\pi = 1$, due to the symmetrical nature of the side-by-side setting, the leader's results overlap that of the follower. By comparison, the results of the leader at $\phi/\pi = 0.5$ tend to coincide with that of the follower at $\phi/\pi = 1.5$.

At staggered arrangement $D > 0$, the follower can take significant advantage of the schooling interaction through various wavelengths, especially at $\lambda \geq 5.6$. This enhancement of the follower's thrust C_{Tm} with λ is most significant when the two foils undulate/pitch in anti-phase $\phi/\pi = 1.0$. For example, as seen in Fig. 5d, a significant difference is observed between the thrust of the follower and that of the leader at the anti-phase $\phi/\pi = 1.0$ cases with close distance $G = 0.25$, $D = 0.25$. At high wavelength λ , the follower's thrust reaches 4.5 times as large as the leader's. Generally speaking, this enhancement effect is activated by a phase difference of $\phi/\pi = 1.0, 1.5$ across various lateral G and front–back D distances, as shown in Fig. 5. The leader–follower thrust

difference decreases when the two swimmers are arranged at a further lateral G and front–back D distance.

Although the follower's thrust is generally larger than the leader's, exceptions are observed in a few cases, as seen in Fig. 5. At $D = 0.25$ with a relatively high wavelength $\lambda > 3$, the thrust upon the leader can become greater than the follower when the two swimmers undulate in-phase $\phi/\pi = 0$. At $D = 0.50$ with $\lambda > 5$, the leader's thrust is higher than the follower at $\phi/\pi = 0$ and 0.5 . At $D = 0.75$ with $\lambda > 5$, the leader's thrust is higher than the follower only at $\phi/\pi = 0.5$. Lateral distance G does not significantly affect this trend. On the contrary, at low wavelength $\lambda \leq 2.0$, the follower always takes a more significant advantage upon the thrust than the leader.

Here, we offer a more general overview regarding the effects of phase difference with the help of Fig. 5. Phase difference ϕ can significantly affect the follower's net thrust while its effects on the leader are less prominent. Furthermore, the effect of the phase difference becomes less significant with the enlargement of the lateral gap G and the front–back distance D , as demonstrated by the converging values of C_{Tm} from Fig. 5a to i. The variation of ϕ is more influential at high wavelength $\lambda > 3$ while being less effective at low wavelength $\lambda \leq 2$.

The net thrust at Strouhal number $St = 0.7$, as seen in Fig. 6, is generally higher than that at $St = 0.4$, across the tested range of wavelengths. At high wavelength $\lambda > 2$, the enhancement of thrust is especially significant, whereas thrust is less sensitive to Strouhal number at low wavelength $\lambda < 1$. Nevertheless, the effects of phase difference and relative distances at $St = 0.7$ is generally coherent with that at $St = 0.4$.

The variation of propulsive force with both wavelength λ and Strouhal number St is further investigated by a heat map at anti-phase $\phi/\pi = 1$ and side-by-side $D = 0$ formations, as seen in Fig. 7. In this symmetrical arrangement, the leader and the follower produce equal net thrust, so Fig. 7 presents only the averaged value. It is seen from the red region that strong propulsive force requires both large wavelength λ and high Strouhal number St . As denoted by the blue region, the net thrust can be negative at low wavelength and low Strouhal number. High St cannot generate strong force if the wavelength is too small $\lambda \leq 1$.

3.3. Individual propulsive efficiency

This subsection discusses the variation of individual propulsive efficiency for the leader or the follower across the tested parametric space. The propulsive efficiency is calculated as net force multiplied by speed divided by power. Maximum individual propulsive efficiency reaches 86% at low wavelength $\lambda = 1.1$ and high Strouhal number with side-by-side schooling and phase difference $\phi/\pi = 0.5, 1.5$.

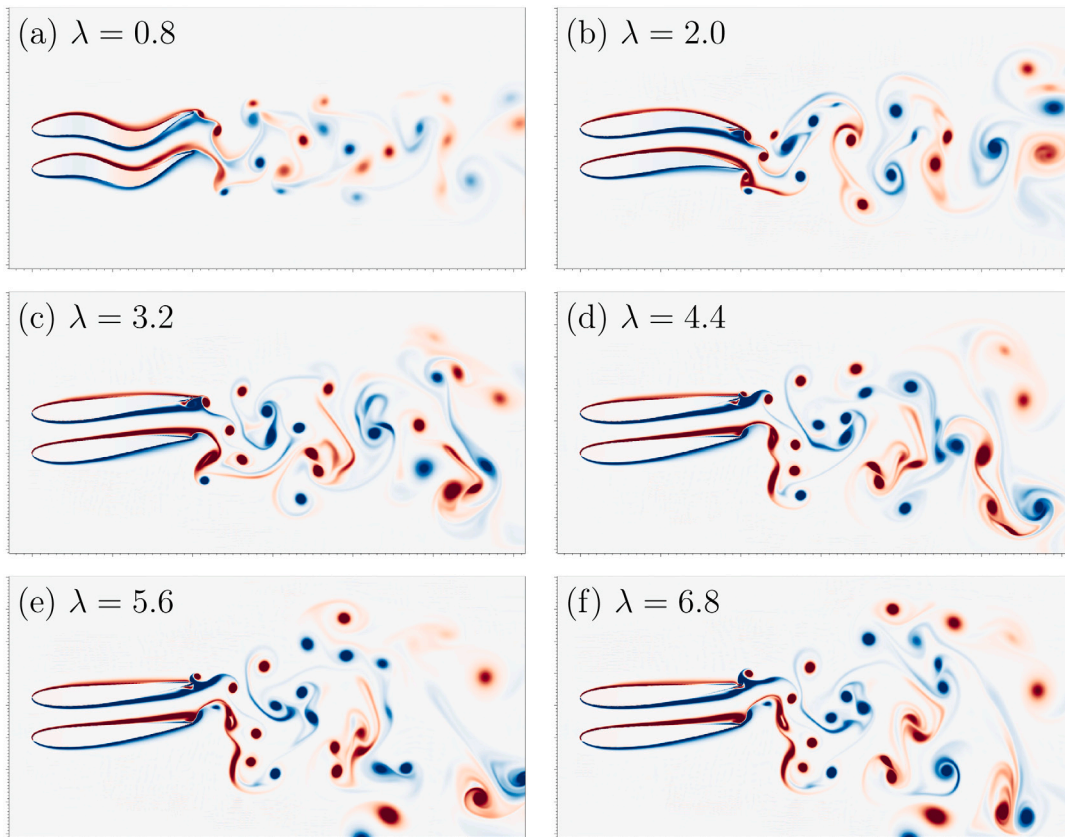


Fig. 13. Variation of hydrofoil geometry and vorticity contours at time $t^*/T = 5$ with $St = 0.4$, $G = 0.25$, $D = 0$, $\phi = 0$, and (a) $\lambda = 0.8$ (b) $\lambda = 2.0$ (c) $\lambda = 3.2$ (d) $\lambda = 4.4$ (e) $\lambda = 5.6$ (f) $\lambda = 6.8$. In general, the intensity and scattering angle of wake vorticity distribution increase with wavelength λ , indicating better stealth performance for low-wave-length swimmers.

At side-by-side arrangement with $St = 0.4$, the *propulsive efficiency* η reaches a maximum at $\lambda = 2$ and then only slightly decreases with wavelength at $\lambda > 2$ and remains almost constant at $\lambda > 5.6$, as shown in Fig. 8a–c. One foil can achieve very high propeller efficiency η at the cost of another foil's η at phase difference $\phi = 0.5\pi$ or 1.5π . This effect is strengthened by stronger flow-mediated interaction through a smaller gap distance G . The difference in efficiency can reach 50% at $G = 0.25$. On the other hand, η can be negative at $\lambda = 0.8$, meaning the leader or the follower foils are not propelling forward.

At staggered arrangement, the individual *propeller efficiency* η for each swimmer generally reaches a minimum at wavelength $\lambda = 0.8$ while peaking at $\lambda = 2.0$, as seen in Fig. 8. The propeller efficiency only slightly changes with wavelength at $\lambda > 2$, where phase lag ϕ affects how λ influences the follower's propeller efficiency $\eta_{follower}$:

- At the in-phase $\phi/\pi = 0$ condition, the follower's efficiency $\eta_{follower}$ significantly decreases with wavelength λ .
- At $\phi/\pi = 0.5$, the negative relationship between λ and $\eta_{follower}$ is less significant than that at $\phi/\pi = 0$.
- At $\phi/\pi = 1.0$ and 1.5 , the result generally remains constant regardless of the variation in λ .

The increase in front-back distance D significantly reduces the propeller efficiency of the follower while slightly increasing the leader's efficiency. In the tested range of values, lateral gap G barely influences the propeller efficiency, being consistent with the conclusion by Li et al. (2020). The follower's efficiency $\eta_{follower}$ is generally higher than the leader's η_{leader} , most significantly at front-back distance $D = 0.25$ and phase lag $\phi/\pi = 1.5$, as demonstrated in Fig. 8a to c; the leader's propeller efficiency can only be slightly higher than the follower's at in-phase condition $\phi/\pi = 0$ and high wavelength $\lambda > 7$. In the present combinations of input parameters, the leader efficiency can be negative

at $\lambda = 0.8$ when the front-back distance is small $D \leq 0.50$, meaning the leader is moving backwards along the flow direction. At $D = 0.75$, the swimmers' efficiency is positive except at $\phi/\pi = 1.0, 1.5$ with low wavelength $\lambda = 0.8$.

At Strouhal number $St = 0.7$, as seen in Fig. 9, the individual propulsive efficiency at low wavelength $\lambda < 2$ is generally much higher than that at $St = 0.4$, whereas at high wavelength $\lambda > 2$, the individual efficiency is reduced for both swimmers. At $St = 0.7$, the maximum propulsive efficiency for both swimmers is achieved at low wavelength $0.6 < \lambda < 1.2$, which is, on the whole, coherent with the biological wavelengths of anguilliform ($\lambda = 0.642$ by Borazjani and Sotiropoulos (2009)) and carangiform ($\lambda = 0.89 - 1.1$ by Borazjani and Sotiropoulos (2009)) swimmers.

3.4. Group propulsive efficiency

In this section, we discuss the group propulsive efficiency to understand the collective performance of schooling in various swimming styles/wavelengths, relative distances and undulation phase differences. Maximum group efficiency occurs at $\lambda = 0.7$ and a high Strouhal number. At a low Strouhal number, the propulsive efficiency for low-wavelength swimmers is more sensitive to relative distance and undulation phase difference. At side-by-side formation with anti-phase and lateral distance $G = 0.35$, the maximum propulsive efficiency of 38% is obtained at $St = 0.45$, $\lambda = 1$. At side-by-side formation with a high Strouhal number, low-wavelength swimmers can achieve a group propulsive efficiency about 15% higher than the high-wavelength swimmers.

At side-by-side arrangement with $St = 0.4$, *group efficiency* reaches a maximum of $\eta_{group} = 31.2\%$ at wavelength $\lambda = 2$ and phase lag $\phi = 0.5\pi$, as seen in Fig. 10a–c. Anguilliform swimming with low

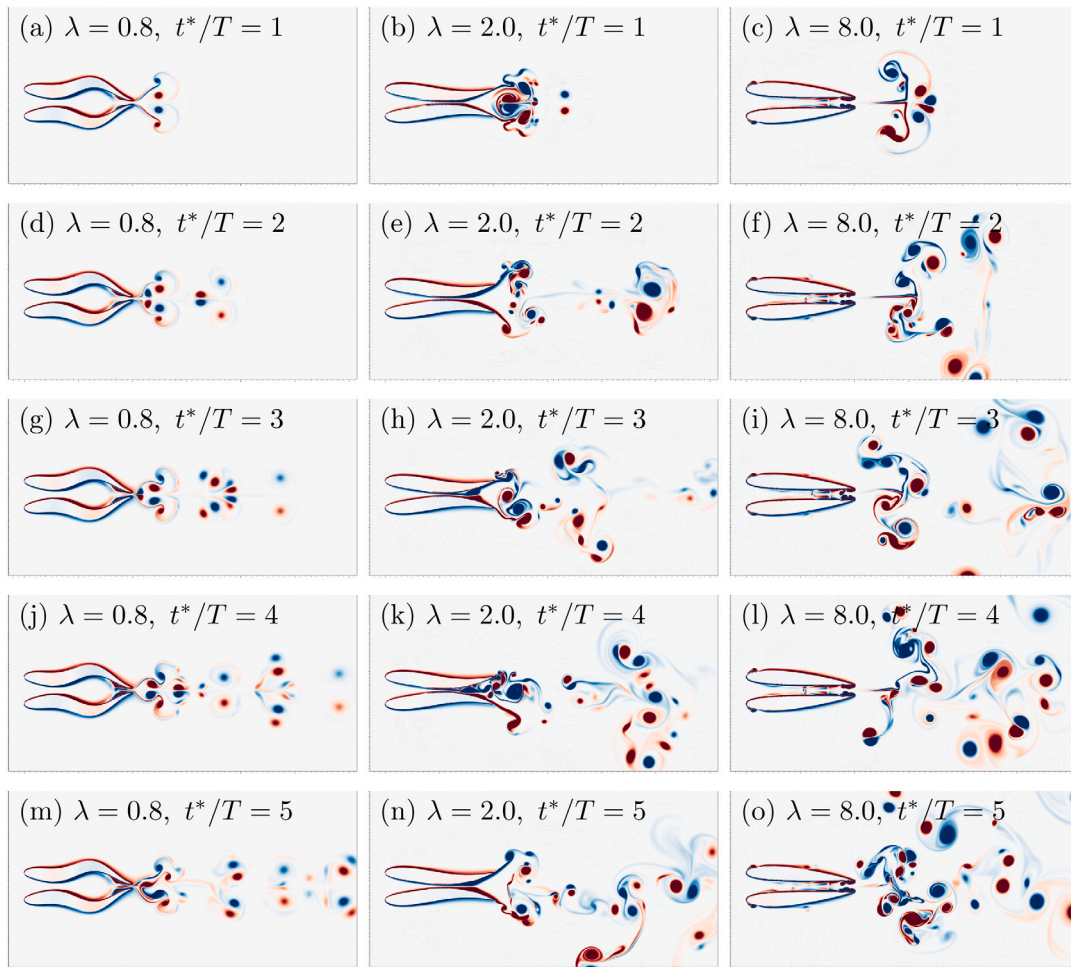


Fig. 14. Vorticity contours and hydrofoil deformation at Strouhal number $St = 0.4$, phalanx arrangement $D = 0$, lateral gap $G = 0.25$, anti-phase $\phi/\pi = 1.0$ at instants (a–c) $t^*/T = 1$ (d–f) $t^*/T = 2$ (g–i) $t^*/T = 3$ (j–l) $t^*/T = 4$ (m–o) $t^*/T = 5$ with various wavelengths (a & d & g & j & m) $\lambda = 0.8$ (b & e & h & k & n) $\lambda = 2.0$ (c & f & i & l & o) $\lambda = 8.0$.

wavelength $\lambda < 1$ can lead to negative group efficiency $\eta_{group} < 0$, indicating that the foils tend to drift along the inlet flow direction; this tendency is strengthened by a narrow gap $G = 0.25$ and in-phase undulation $\phi = 0$. For Carangiform swimming at higher λ , the group efficiency slightly increases with the gap distance, especially for the in-phase $\phi = 0$ scenarios. The group efficiency is highly consistent for phase lag $\phi = 0, \pi$ and $\phi = 0.5\pi, 1.5\pi$, at $G = 0.30, 0.35$ and high wavelength $\lambda > 5$.

For schooling short-wavelength swimmers, it can be critical to keeping an appropriate front-back distance D , which may even reverse the collective propulsive direction of the swimmer group; in contrast, the schooling performance for high-wavelength swimmers $\lambda > 6$ is more stable; its group efficiency does not vary significantly with phase lag ϕ and front-back distance. At staggered arrangement, the group efficiency η_{group} represents the effectiveness of energy conversion from lateral undulation to thrust propulsion for the two interacting swimmers as a minimal school. The group efficiency η_{group} reaches a minimum at $\lambda = 0.8$, peaks at $\lambda = 2.0$, and then gradually approaches a specific value at large wavelength $\lambda = 8.0$; this pattern can be observed across all simulated cases. The group efficiency η_{group} reaches maximum at 33.3% with front-back distance $D = 0.75$ and wavelength $\lambda = 2.0$. In the explored parametric space, η_{group} generally increases with lateral gap G and front-back distance D across various wavelengths λ , as seen in Fig. 10. At low wavelength $\lambda = 0.8$, the group efficiency is especially sensitive to front-back distance D but less sensitive to lateral distance G , being consistent with the conclusions by Li et al. (2020). The increase of front-back distance D and lateral gap G leads

to reduced sensitivity regarding phase lag ϕ across various wavelengths $\lambda = 0.8 - 8$, as seen in Fig. 10i for the almost overlapped lines; this trend corresponds to the reduced difference in propeller efficiency η between the leader and the follower, as seen in Fig. 10, implying reduced flow-mediated interference between the two swimming foils. At low wavelength $\lambda = 0.8$, the negative group efficiency is observed at front-back distance $D \leq 0.50$ but not found in cases with $D = 0.75$.

At high Strouhal number $St = 0.7$, the group propulsive efficiency reaches the maximum at low wavelengths $\lambda < 1$, which is in contrast with that at $St = 0.4$, where the group efficiency is obtained at intermediate wavelength $\lambda = 2$. At high Strouhal number $St = 0.7$ with side-by-side arrangement $D = 0$ in Fig. 11a, the highest group propulsive efficiency is achieved at $\lambda = 0.7$ when the two swimmers undulate in anti-phase $\phi/\pi = 1$. At high Strouhal number $St = 0.7$ with staggered arrangement $D = 0.75$ in Fig. 11b, the group efficiency is no longer significantly affected by the phase differences.

We draw a heat map to discuss how propulsive efficiency varies with Strouhal number and wavelength at anti-phase and side-by-side formation, as seen in Fig. 12. At this symmetrical condition, the two swimmers share the same propulsive efficiency, so Fig. 12 presents the averaged value. For side-by-side schooling with anti-phase, the high-efficiency $\eta > 35\%$ is obtained at $\lambda \approx 1$, $St = 0.4 - 0.7$, as seen in Fig. 12. A low Strouhal number is more energy-conserving for large wavelength swimmer schools. The green star * marker denotes the location for maximum efficiency 38% at $St = 0.4$ and $\lambda = 1$. High efficiency $\eta > 35\%$ is achieved in a narrow band with $\lambda \approx 1$, $St = 0.4 - 0.7$. At high wavelength, relatively low Strouhal number St is more efficient, as seen

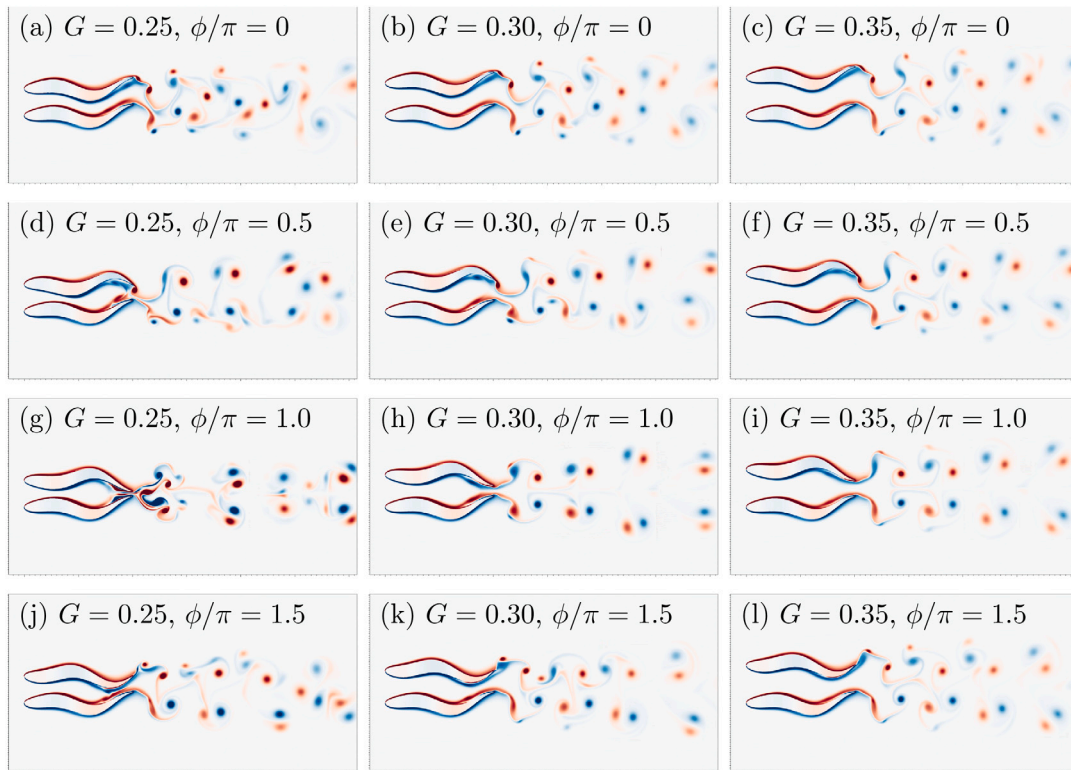


Fig. 15. Vorticity contours and hydrofoil deformation at Strouhal number $St = 0.4$, instant $t^*/T = 5$ with $G = 0.35$, $D = 0$, (a-c) $\phi/\pi = 0$ (d-f) $\phi/\pi = 0.5$ (g-i) $\phi/\pi = 1.0$ (j-l) $\phi/\pi = 1.5$. (a & d & g & j) $G = 0.25$ (b & e & h & k) $G = 0.30$ (c & f & i & l) $G = 0.35$. At low wavelength $\lambda = 0.8$, the distribution of vortices is subtly affected by the gap distance and phase difference; concentration of dynamic energy is discovered at low gap distance for anti-phase cases.

in the upper left corner. For the cases with negative net thrust, $C_{Tm} < 0$, the efficiency is drawn as zero.

3.5. Flow symmetry and its breaking with side-by-side arrangement

This subsection discusses the unique flow patterns at side-by-side formation: symmetrical flow structure and its breakage with various swimming styles/wavelengths. The distribution of vorticity ω^* is observed to reveal the general flow structure underlying the abovementioned patterns regarding the thrust and swimming economy of the schooling hydrofoils. Wake vortices are also examined due to their implications for the stealth capacity of schooling swimmers. The main focus is on the effects of swimming styles/wavelengths. Flow instability occurs at a small gap distance $G \leq 0.3$ and high wavelength $\lambda > 4$, leading to chaotic flow structure and resultant force. The rest of the parametric space produces a periodical flow structure. In addition, a detailed examination of fluid–structure interaction in a specific period at a side-by-side arrangement can be found in Appendix C.

The separated discussion of side-by-side arrangement is justified by the rich physics due to its distinguished symmetrical flow structure and potential occurrence of symmetry breaking (Gungor and Hemmati, 2020) and by the observation of fish's tendency to form a phalanx formation in a free-stream flow (Ashraf et al., 2017). It is also a curious question that how the variation of wavelength affects the flow symmetry and wake patterns.

Wavelength λ is positively correlated with shed vortices' intensity and scattering area, as seen in Fig. 13. At low wavelength $\lambda = 0.8$ in Fig. 13a, the vortex shedding is distributed in a narrow band at the downstream side of the schooling foils, indicating better stealth performance for low-wave-length swimmers. With a longer wavelength λ , the wake vortices can disturb a larger area, making the flow structure increasingly complicated. One vortex dipole, i.e. a pair of opposite-sign vortices, is generated in each undulation cycle. The interaction between

the shed dipoles becomes more unsteady with a larger wavelength λ (see Fig. 13) and a shorter gap distance G (see Fig. 15).

At phalanx arrangement $D = 0$ and anti-phase $\phi/\pi = 1$, vorticity distribution is examined in Fig. 14 to seek the underlying mechanism of the irregular force output. Here, the two swimmers form a mirror symmetry geometry at any moment during the undulation process. However, the consequent flow pattern does not always remain symmetrical through the development of time; this symmetry-breaking phenomenon tends to occur with a higher wavelength. At low undulation wavelength $\lambda = 0.8$, the flow pattern is symmetrical in the initial periods, and the symmetry breaking only gradually becomes observed after the sixth period of undulation $t^*/T = 6$. At high wavelength $\lambda \geq 2.0$, the wake flow becomes highly irregular within merely 1 or 2 initial periods of undulation; the chaotic flow structure occurs very close to the tails of the undulating fish, thus causing the fluctuation in the output thrust. Across various λ , the propulsive performance measurements such as thrust are highly consistent with the symmetric features of the near field wake structure. Gungor and Hemmati (2020) also discovered similar symmetry-breaking phenomenon of two hydrofoils pitching in anti-phase, though only with infinite wavelength $\lambda = +\infty$ at $Re = 4000$ and $St = 0.25 - 0.5$. In summary, the irregularity of the flow structure tends to increase with undulation wavelength λ .

At low wavelength λ , the gap distance G and phase difference ϕ can affect the skewness, symmetry and regularity of the wake pattern, as demonstrated in Fig. 15. It is interesting to observe that at $\phi/\pi = 0.5$ and $\phi/\pi = 1.5$, the vortex shedding direction is slightly skewed towards the right and left sides of the swimming direction, respectively. At $\phi/\pi = 1.0$, the flow structure is symmetrical due to the anti-phase undulation of the hydrofoils. The intensity of the vortices decreases with a larger gap distance G . With a small gap distance $G = 0.25$, the vortices are distributed in a narrower band of wake flow, i.e. the dynamic energy is more concentrated at $G = 0.25$; in contrast, the decrease in gap distance G is relatively less effective in cases with other

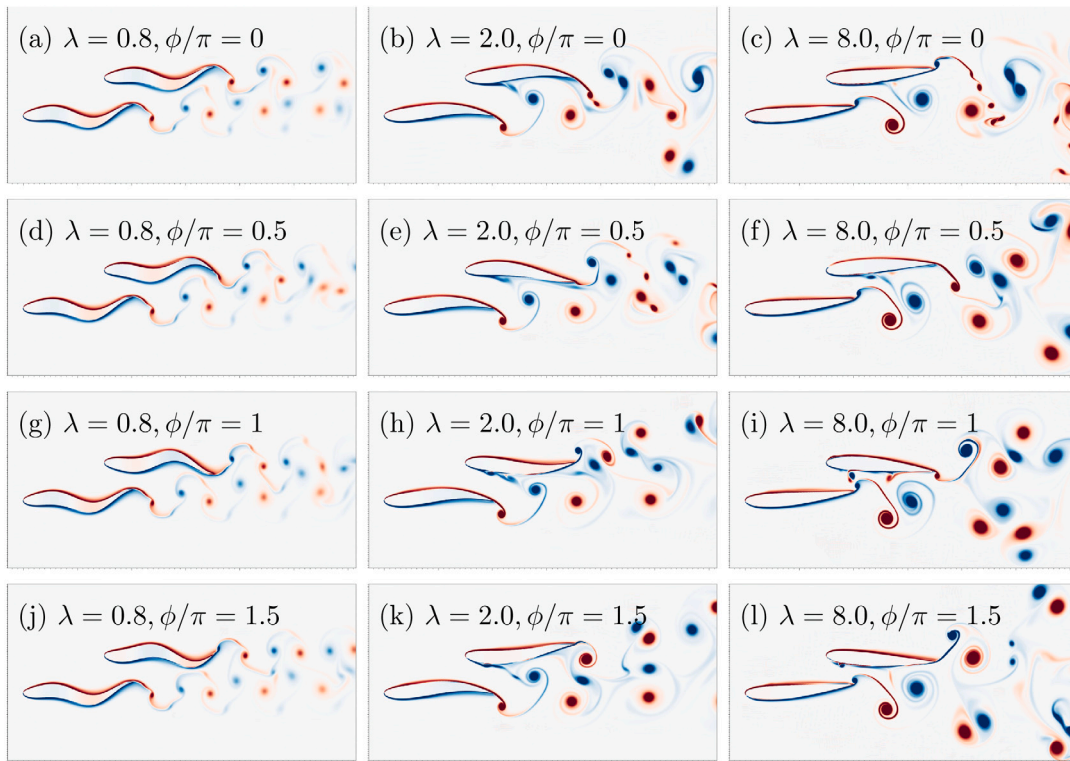


Fig. 16. Vorticity contours and hydrofoil deformation at instant $t^*/T = 5$ at Strouhal number $St = 0.4$, relative distances $G = 0.35$, $D = 0.75$ and a variety of phase difference (a-c) $\phi/\pi = 0$ (d-f) $\phi/\pi = 0.5$ (g-i) $\phi/\pi = 1.0$ (j-l) $\phi/\pi = 1.5$ and various wavelengths (a & d & g & j) $\lambda = 0.8$ (b & e & h & k) $\lambda = 2.0$ (c & f & i & l) $\lambda = 6.8$.

phase differences ϕ . At $\phi/\pi = 0$, the mixture of vortices is observed at $G = 0.25$, whereas at $G \geq 0.30$, the mixture does not occur. In summary, at low wavelength $\lambda = 0.8$, the distribution of vortices is subtly affected by the gap distance and phase difference; concentration of dynamic energy is discovered at low gap distance and when the two hydrofoils swim in anti-phase.

3.6. Lagged vortex interaction with staggered arrangement

The investigation of the fluid–structure interaction mechanism for staggered arrangement $D > 0$ is to understand the effects of swimming styles, i.e. wavelengths, based on the vortex phase matching mechanism proposed by Li et al. (2020). In addition, a detailed examination of fluid–structure interaction in a specific period at staggered arrangement can be found in Appendix D.

The wavelength λ and the phase lag ϕ influence the vortex strength and shedding pattern in different ways, as seen in Fig. 16. The general wake flow pattern is not significantly affected by the phase difference ϕ ; this also corresponds to the results in Fig. 10. At $\lambda = 0.8$, the general vortex shedding pattern is barely affected by the variation in phase difference ϕ . The dipoles shed by the two foils hardly interact, especially when the two foils swim in-phase $\phi = 0$, as seen in Fig. 16a. The dipoles steadily drift downstream, meaning the streaming direction is stable as well. At $\lambda = 2.0$, significant interference between the dipoles leads to irregular flow structure in the downstream area of the two foils. However, in the area between the two foils, the flow structure is regular and predictable, indicating that the interaction between the two foils should essentially be periodical despite the complex pattern downstream. Phase lag ϕ can significantly affect the flow structure immediately downstream of the follower foil. At $\lambda = 8.0$, the flow pattern is similar to that at $\lambda = 2.0$ but with a larger scattering area in the wake.

In order to examine the inter-relationship between wavelength λ , front–back distance D , and wake flow structure, we draw the vorticity contours across various wavelengths λ and front–back distances D , as

seen in Fig. 17. At front–back distance $D = 0.25$, as seen in Fig. 17a–c, the vortex dipoles shed by each hydrofoil do not mix in the wake flow, but bifurcating towards two distinct directions, forming an angle with a near-perfect mirror symmetry about the centreline. This symmetrically stable flow structure persists despite the variation of wavelengths λ . Such near-symmetrical patterns were only observed in cases with *phalanx* arrangement $D = 0$ and *anti-phase* $\phi/\pi = 1$ condition, e.g. cases discussed in Section 3.5 and the results from another paper focusing on wake symmetry by Gungor and Hemmati (2020). It is therefore interesting to observe a very similar pattern at a *staggered* placement $D = 0.25$ with *in-phase* $\phi/\pi = 0$ undulations. To explain this phenomenon, we further examine the underlying hydrodynamic mechanism. The front–back distance of $D = 0.25$ causes the positive vortex from the present half-cycle of the follower to collide with the negative vortex from the previous half-cycle of the leader. These two vortices collide without merging due to their opposite rotating direction, thus pushing each other away while drifting downstream, eventually leading to a steady flow structure with a certain angle. This periodic flow pattern does not lead to a superior thrust or locomotion efficiency as previously discussed, yet it may contain implications for the stealth capacity of the swimmers. As for cases at $D \geq 0.50$, the wake flow structure is more irregular due to unsteady interaction among dipoles, e.g. some vortices merge to form a larger one. The overall vorticity strength and the degree of irregularity both increase with the wavelengths λ . Although the wake flow is irregular for the cases at $D \geq 0.50$, the flow structure near the two foils is mainly predictable, especially in the area between the two foils.

4. Conclusion

While fish schooling with constant swimming speed is generally well researched (Weihs, 1973, 1975; Daghooghi and Borazjani, 2015; Ashraf et al., 2016; Li et al., 2020), far less is known for accelerated schooling with various swimming styles. The main contribution of the present paper is to systematically examine the hydrodynamic

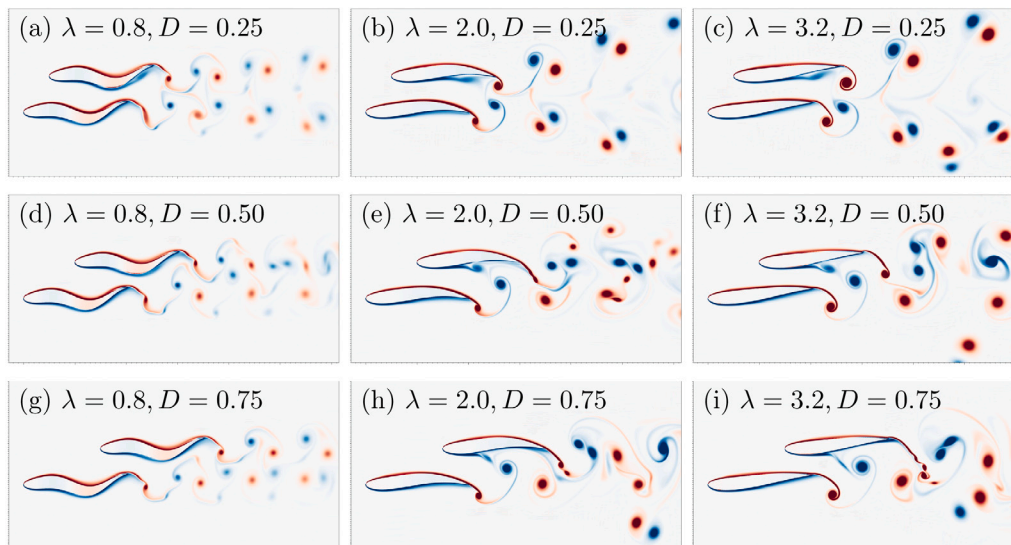


Fig. 17. Vorticity contours and hydrofoil deformation at instant $t^*/T = 5$ with $St = 0.4$, $G = 0.35$, $\phi = 0$, (a-c) $D = 0.25$ (d-f) $D = 0.50$ (g-i) $D = 0.75$ (a & d & g) $\lambda = 0.8$ (b & e & h) $\lambda = 2.0$ (c & f & i) $\lambda = 3.2$.

performance of a minimal school accelerating with various swimming styles/wavelengths. Here, we investigate how swimming style and schooling affect the linear acceleration of two wavy hydrofoils at various wavelengths $\lambda = 0.8 - 8$, front-back distance $D = 0, 0.25, 0.5, 0.75$, Strouhal number $St = 0.4, 0.7$, phase difference $\phi/\pi = 0, 0.5, 1, 1.5$, and lateral gap distance $G = 0.25, 0.3, 0.35$ with fixed Reynolds number $Re = 5000$ and maximum amplitude $A_{max} = 0.1$. In total, 591 combinations were simulated by the ConstraintIB module of IBAMR. The swimmers with various wavelengths in this paper are inspired by BCF swimmers in nature with various swimming styles.

In the present paper, we found that:

1. The highest group propulsive efficiency is obtained at low wavelength $\lambda < 1.2$. High-wavelength schools produce stronger net thrust, especially at a side-by-side arrangement with anti-phase coordination. However, they cannot obtain the best locomotion efficiency.
2. Across various wavelengths, the side-by-side arrangement is a stable formation during acceleration, given the maintenance of appropriate lateral distance.
3. Tuning phase difference can optimise the follower's net thrust and efficiency. The phase-tuning effect is enhanced by short front-back distances and long wavelengths. A larger front-back distance changes the optimal phase difference for the best thrust performance, consistent with a previous report (Li et al., 2020).
4. The increase in the relative distance reduces the follower's additional thrust and efficiency, but increases the group propulsive efficiency across various wavelengths.
5. At a large relative distance, typically at $D \geq 0.75$, the two swimmers' thrust and propulsive efficiency tend to collapse into similar values with marginal influence from the phase difference; in other words, the schooling effect fades.
6. At side-by-side formation with a high Strouhal number $St = 0.7$, a critical wavelength $\lambda = 1.1$ is discovered that below which, the anti-phase schooling yields better group efficiency, whereas beyond which, in-phase schooling is more efficient.
7. The high-efficiency $\eta > 35\%$ region is located at $\lambda \approx 1$, $St = 0.4 - 0.7$, consistent with swimmers in nature. Low Strouhal number $St < 0.4$ can be more efficient for high-wavelength swimmers.
8. Although the low-wavelength swimmers underperform long-wavelength ones at low Strouhal number $St = 0.4$ with low propulsive efficiency, increasing the St to 0.7 can easily enhance the efficiency for low-wavelength swimmers regardless of the

front-back and lateral distances. In other words, the effects of swimming style and Strouhal number outweigh the schooling interaction.

9. While schooling together, the low-wavelength swimmers tend to produce a more stable wake flow than the high-wavelength swimmers, disturbing less area of the fluid. This implies a better stealth performance for low-wavelength swimmers.
10. Symmetrical flow occurs when swimmers are placed side-by-side and undulate in anti-phase. High wavelength encourages the onset of symmetry breaking, especially at a small lateral gap.

In a nutshell, the linear acceleration of a minimal school can be affected by the swimming styles and the schooling parameters. Low and high wavelengths correspond to advantageous propulsive efficiency and thrust, respectively, which is consistent with the single swimmer scenario (Thekkethil et al., 2018). Appropriate schooling distances and phase differences may further enhance the locomotion advantages for either the individuals or the group. Furthermore, certain swimming styles and schooling parameters reduce the scattering of the vortices and, thus, better stealth capacity. Since high- and low-wavelength swimming styles have their advantages and disadvantages, the present study cannot conclude which swimming style/wavelength is most suited for schooling. Nevertheless, the present results can be helpful for the future design of underwater propellers, which can be designed in a parametric space more comprehensively than the swimmers in the nature, or may even employ multiple hydrofoils with tunable wavelengths.

5. Limitations and future works

In the present study, the simulation cases are all based on the simplified geometry of NACA0012. Although this study draws inspiration from the anguilliform, carangiform and thunniform swimmers in nature, these swimmers not only differ in undulation wavelength but also in the body geometry and structure (Borazjani and Sotiropoulos, 2008, 2009, 2010). So the present results may be less applicable to the BCF swimmers in nature, but more to the biomimetic propellers in engineering applications. The Reynolds and Strouhal numbers are limited to $Re = 5000$ and $St = 0.4, 0.7$ to focus on the effects of swimming modes and schooling for accelerating swimmers. The number of values for relative distances is constrained due to computational power limitations. A larger quantity of simulations may yield more insights in the future. The present study still cannot explain the lack

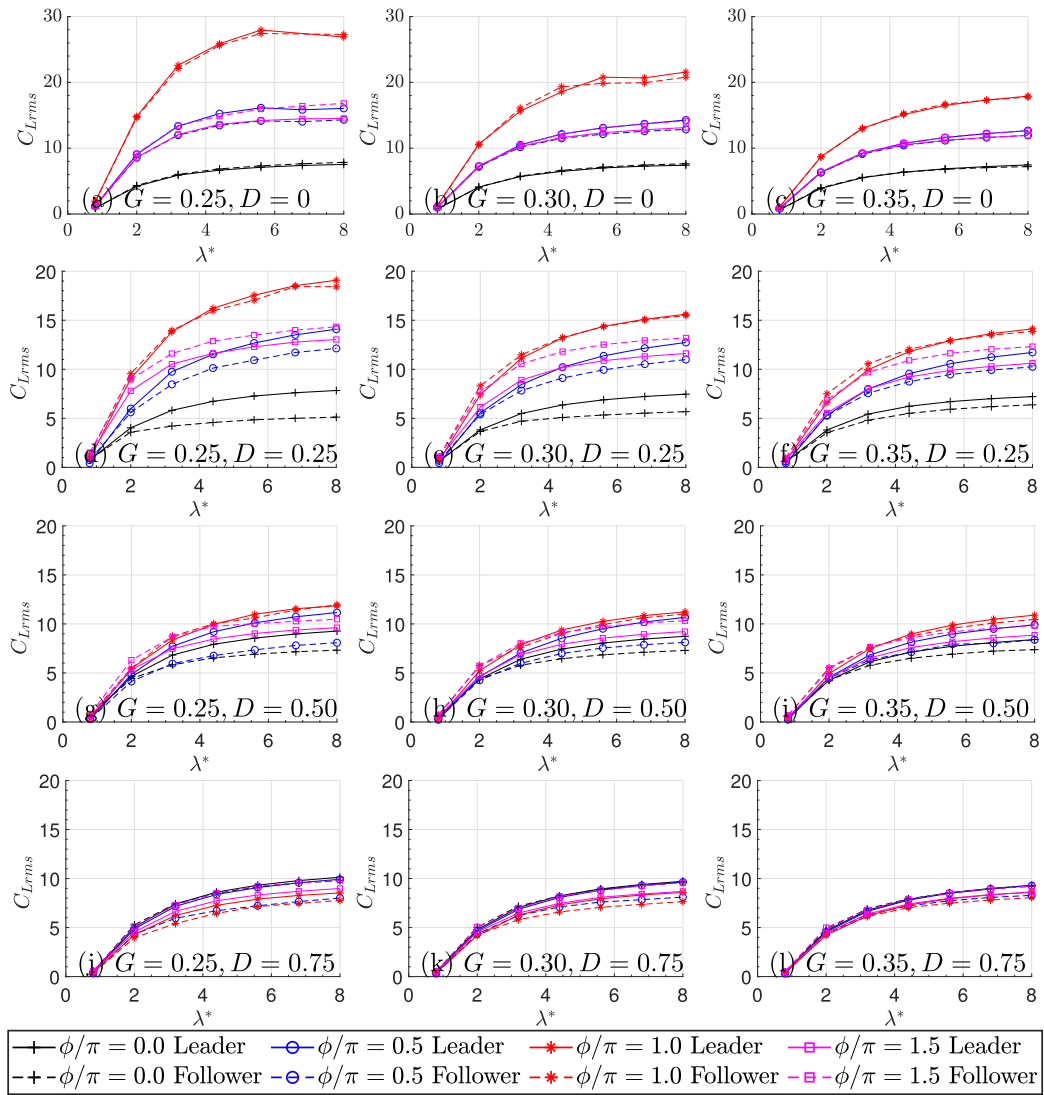


Fig. A.18. Variation of root mean square of lateral force C_{Lrms} for both leader (solid lines) and follower (dashed lines) hydrofoils at Strouhal number $St = 0.4$, a series of wavelength $\lambda = 0.8 - 8.0$, leader–follower phase difference $\phi/\pi = 0, 0.5, 1.0, 1.5$ (denoted by marker types), front–back distance (a–c) $D = 0$, (d–f) $D = 0.25$, and (g–i) $D = 0.50$, (j–l) $D = 0.75$; lateral gap distance at (a & d & g & j) $G = 0.25$, (b & e & h & k) $G = 0.30$, (c & f & i & l) $G = 0.35$.

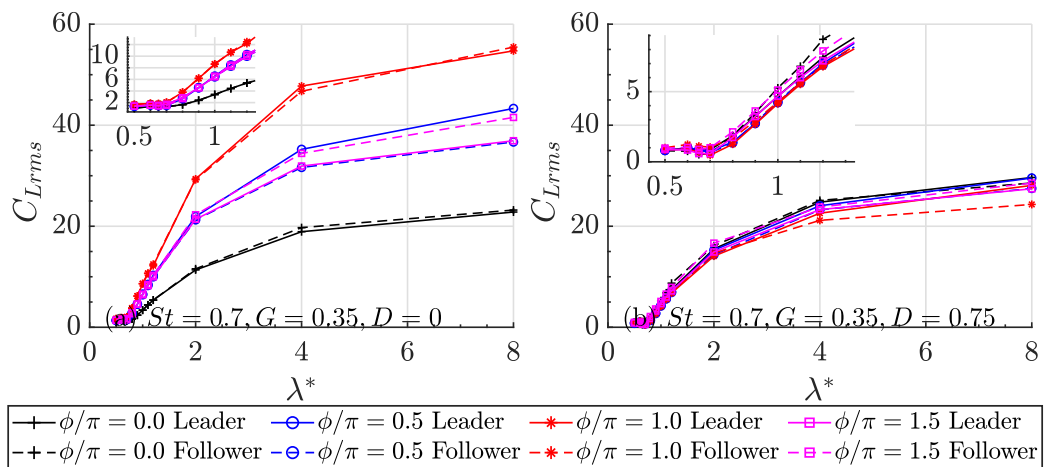


Fig. A.19. Variation of root mean square of lateral force C_{Lrms} for both leader (solid lines) and follower (dashed lines) hydrofoils at Strouhal number $St = 0.7$, a series of wavelength $\lambda = 0.8 - 8.0$, leader–follower phase difference $\phi/\pi = 0, 0.5, 1.0, 1.5$ (denoted by marker types), front–back distance (a) $D = 0$, (b) $D = 0.75$.

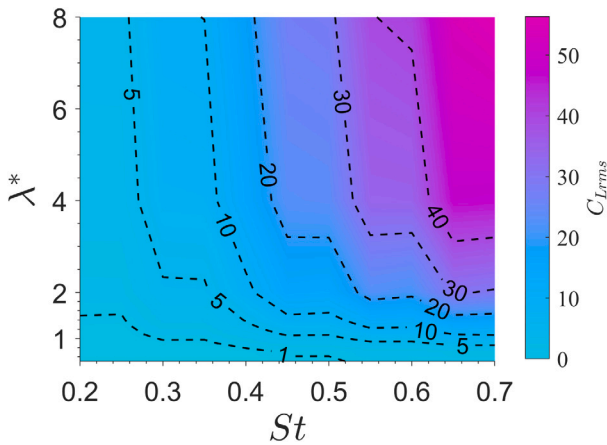


Fig. A.20. The heat map denotes the lateral force C_{Lrms} as a function of Strouhal number $St = 0.2 - 0.7$ and wavelength $\lambda = 0.5 - 8$ at anti-phase $\phi/\pi = 1.0$, side-by-side formation $D = 0$, lateral gap distance at $G = 0.35$. The lateral force is positively correlated with wavelength λ and Strouhal number St .

of reports on anguilliform schooling swimmers, which may require future multidisciplinary studies. In the future, we intend to investigate further the schooling mechanism for different swimming styles in 3D simulations and robotic fish experiments. Further discussion regarding tethered and self-propelling conditions can be found in [Appendix E Tethered and self-propelling conditions](#).

CRediT authorship contribution statement

Zhonglu Lin: Conceptualization, Methodology, Validation, Formal analysis, Investigation, Data curation, Writing – original draft, Writing – review & editing, Visualization, Funding acquisition. **Amneet Pal Singh Bhalla:** Software, Validation. **Boyce E. Griffith:** Software. **Zi Sheng:** Software. **Hongquan Li:** Resources. **Dongfang Liang:** Writing – review & editing. **Yu Zhang:** Supervision, Project administration, Funding acquisition.

Declaration of competing interest

The authors declare that they have no known competing financial interests or personal relationships that could have appeared to influence the work reported in this paper.

Data availability

Data will be made available on request.

Acknowledgements

We acknowledge the help from Yu Jiang for data processing. We appreciate the suggestions from the reviewers of Ocean Engineering, which have improved this paper. This work was funded by China Postdoctoral Science Foundation under Grant Number 2021M691865 and by Science and Technology Major Project of Fujian Province (China) under Grant Number 2021NZ033016. A.P.S.B acknowledges support from the US National Science Foundation award OAC 1931368. This work was financially supported by the National Natural Science Foundation of China under Grant Number 12074323 and 42106181, the Special Fund for Marine and Fishery Development of Xiamen under Grant Number 20CZB015HJ01, the Guangzhou Science and Technology Foundation under Grant Number 202102020901, the China National Postdoctoral Program for Innovative Talents under Grant Number BX2021168 and the Outstanding Postdoctoral Scholarship, State Key Laboratory of Marine Environmental Science at Xiamen University.

Appendix A. Lateral force coefficient

Here we discuss the variation of the lateral force C_{Lrms} , which is linked to the work done from the undulating foil to the incompressible fluid. At Strouhal number $St = 0.4$, the RMS of lateral force C_{Lrms} increases monotonically with wavelength λ despite the variation of other parameters, as seen in [Fig. A.18](#). The lateral force dramatically increases with the wavelength λ , reaching as high as $C_{Lrms} = 18$ for both swimmers, at short distance $G = 0.25$, $D = 0.25$ and anti-phase $\phi/\pi = 1$, as shown in [Fig. A.18a](#). Regarding the effects of the phase difference ϕ , the lateral force C_{Lrms} reaches a minimum when the two hydrofoils swim in-phase $\phi/\pi = 0$ while reaching maximum at anti-phase $\phi/\pi = 1$ condition with front-back distance $D \leq 0.50$, as seen in [Fig. A.18](#). However, at $D = 0.75$, this relationship is reversed that the minimal C_{Lrms} is found at anti-phase condition. In contrast, the maximal C_{Lrms} are discovered in in-phase scenarios. This observation can be postulated to be related to vortex shedding and its impingement upon the follower. As the distances G and D increase, the phase difference ϕ becomes less influential upon the lateral force C_{Lrms} for both the leader and the follower, as shown in [Fig. A.18](#). With the increase of lateral gap G and front-back distance D , the difference of lateral force C_{Lrms} between the leader and the follower becomes smaller; as the lateral gap increases from $G = 0.25$ to 0.35 and the front-back distance rises from $D = 0.25$ to 0.75 , the leader-follower lateral force difference decreases from 2.5 to 0.5 , as seen in [Fig. A.18a](#) to *i*. Compared with the significant leader-follower difference for the thrust C_{Tm} previously discussed, the leader-follower discrepancy in lateral force C_{Lrms} is relatively small, especially at short distances $G = 0.25$, $D = 0.25$, indicating the thrust is more sensitive to the schooling effect than the lateral force, across the tested wavelengths. At a higher Strouhal number $St = 0.7$, the lateral force is significantly increased, as seen in [Fig. A.19](#). Specifically for the side-by-side formation and anti-phase, we draw a heat map to demonstrate the variation of lateral force with Strouhal number and wavelength, as seen in [Fig. A.20](#). It can be more clearly seen that the lateral force is positively correlated with wavelength λ and Strouhal number St .

It can be summarised that the variation of lateral force demonstrates a relatively simple pattern:

1. The lateral force increases monotonically with the wavelength for both schooling members.
2. The lateral force is generally equivalent when the two foils undulate in anti-phase, regardless of relative distances.
3. A larger Strouhal number can significantly enhance the lateral force.

Appendix B. Time history

In the present study, most of the cases can reach a periodical state, as seen in [Fig. B.21a](#). At high wavelength, the flow structure can be unsteady, causing fluctuation in the time history, as seen in [Fig. B.21b](#); however, the general force amplitude can still be characterised by the last few periods. As a result, the present study uses the last three periods out of at least ten periods to calculate the mean thrust, root mean square of the lateral force, and other representative values.

Appendix C. Flow variation in a typical cycle at side-by-side arrangement

This section scrutinises, in a typical cycle of undulation, how the swimming style affects the flow structure, vortex shedding and the corresponding thrust and lateral force at side-by-side and staggered arrangement. For the anti-phase $\phi/\pi = 1$ scenarios, the results are analysed in detail for wavelengths $\lambda = 0.8, 2.0, 8.0$ with the help of [Figs. C.22 to C.24](#), where the time history of net thrust C_T upon the foils are examined together with vorticity distribution at corresponding

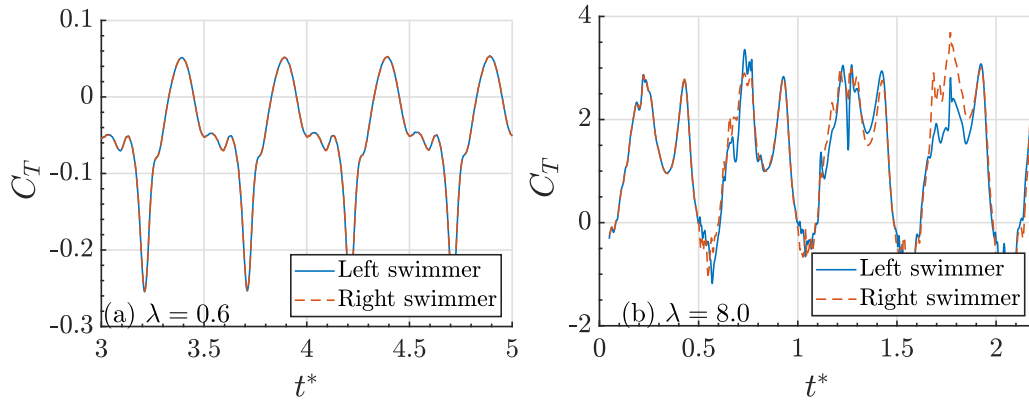


Fig. B.21. Time history of thrust coefficient C_T for both leader (solid lines) and follower (dashed lines) hydrofoils at Strouhal number $St = 0.4$, leader–follower phase difference $\phi/\pi = 1.0$ (denoted by marker types), side-by-side arrangement $D = 0$, wavelength (a) $\lambda = 0.6$ (b) $\lambda = 8.0$. At high wavelengths, the flow structure can be unsteady, causing fluctuation in the time history; however, the general force amplitude can still be characterised by the last few periods.

instants within one period of deformation. This configuration of $D = 0$ and $\phi/\pi = 1$ is justified by the observation from Ashraf et al. (2017) that schooling fish tend to form a simple side-by-side pattern with the characteristics of synchronised tail-beating with either in-phase or anti-phase swimming modes. Ashraf et al. (2017) previously observed the fish schooling of a single wavelength of red nose tetra *Hemigrammus Rhodostomus*. Strong vortex interaction has been identified at low gap distance $G = 0.25$ and anti-phase cases $\phi/\pi = 1$. We thus further investigate the effects of wavelengths across typical values $\lambda = 0.8, 2, 8$.

The swimming deformation of the foils is an overlap of both lateral pitching motion and travelling sinusoidal wave. At low wavelength $\lambda = 0.8$, the component of the travelling wave becomes more significant with a wavy appearance shown in Fig. C.22. For the single foil swimming cases (Thekkethil et al., 2018), two vortices of opposite signs are shed in each cycle of undulation. In the present case of two side-by-side foils undulating in anti-phase, strong but symmetrical interference is discovered between the vortices generated by each foil, as seen in Fig. C.22. In the *outward* movement of the swimmers' tail tips, as demonstrated in Fig. C.22a–d, each of the two foils produces a vortex of opposite signs, temporarily forming a vortex pair. Meanwhile, the travelling wave deforming the foils propels the fluid between the two foils, pushing these two vortices downstream. During the *inward* phase of the tail tip movement, i.e. Fig. C.22e–h, each foil sheds one more vortex, which, in the next cycle, gradually forms a vortex dipole by pairing with the previous vortex from the same foil, i.e. Fig. C.22a–d. Eventually, the vortex dipoles from each of the two foils repel their counterparts and travel laterally away from each other, forming a highly symmetrical pattern of vortex dipoles in the downstream area. Corresponding to the high level of symmetry in flow structure, the thrust of the two foils are identical through the variation of time $C_{T,1} = C_{T,2}$, indicating the two foils reach a stable formation and propel in a synchronised manner, as seen in Fig. C.22i and j. The lift force of the two foils are opposite to each other as $C_{L,1} = -C_{L,2}$, which also periodically switches direction; so the two foils repel each other at instants Fig. C.22a–d while attracting each other at instants Fig. C.22e–h.

At intermediate wavelength $\lambda = 2$, the highest energy efficiency can be obtained, as previously discussed. Here, we further analyse its vorticity contour to study its flow structure and flow-mediated interaction. Similar to low wavelength cases, the tail tip movement governs the generation of vortices. Each foil generates a vortex in the near-tail region when the tail tip moves *outward* in Fig. C.23c–f. During the *inward* phase shown in Fig. C.23g–h and Fig. C.23a–b, the vortices on each foil's outer side are also generated. The vortex dipoles eventually form a streaming direction that points downstream,

enhancing the propulsion of the swimmers. It is also interesting to notice that at $\lambda = 2$, the velocity of shed vortex dipoles is almost two times that at $\lambda = 0.8$. The thrust and lateral force follow the same pattern as the low wavelength scenario at $\lambda = 0.8$.

At large wavelength $\lambda = 8.0$, the swimming motion of the foils consists mainly of pitching rather than undulation, as seen in Fig. C.24. Due to the anti-phase setting $\phi/\pi = 1$, the pitching of two swimmers periodically switches between *outward* and *inward* movement. The *outward* motion creates a vortex dipole between the tails of the two swimmers, as shown in Fig. C.24a–d. During the outward movement, the dipole stays near the tail region despite the streaming flow. The *inward* motion, i.e. Fig. C.24e–h, then pushes out the vortex dipole while creating two vortices at each outer side of the two foils. As a result, a strong jet flow is also produced. In this period of motion, the flow symmetry gradually breaks, causing an increasingly complicated flow structure, which corresponds to the unsteady thrust $C_{T,m}$ and lateral $C_{L,rms}$ force as seen in Fig. C.24i and j. The symmetry breaking occurs at the instant $t^*/T = 2.25$ in Fig. C.24c, where the large vortex dipole is broken into multiple small vortices. In addition to the near-tail vortex dipole, two relatively small vortices emerge from each foil's outer sides and then travel along each foil's surface. The generation of these outer minor vortices starts to generate at the later phase of the inward pitching movement at instant $t^*/T = 2.75$ in Fig. C.24g and instant $t^*/T = 2.875$ in Fig. C.24h, and then remains almost static in the outward pitching motion at Fig. C.24a–d; the displacement of these minor vortices takes place during the inward motion at Fig. C.24e–h. This phenomenon is only observed in the anti-phase cases with the high wavelength in the tested parametric space. In addition, the broken symmetry corresponds to the irregular thrust at the anti-phase condition, as depicted in Fig. 5a and b.

Appendix D. Flow variation in a typical cycle at staggered arrangement

This section scrutinises, in a typical cycle of undulation, how the swimming style affects the flow structure, vortex shedding, and the corresponding thrust and lateral force at the *staggered* arrangement.

At $D = 0.75$, $\lambda = 0.8$, the wake vorticity pattern looks as if each of the two foils swims as a single foil, i.e. interference between the wake flows by two foils are visibly insignificant, as viewed in Fig. D.25a–h. However, a significant discrepancy of thrust C_T is discovered between the two swimmers; the leader's thrust is generally negative, whereas the follower's is on the whole positive, as seen in Fig. D.25i and j, indicating that the two foils are attracted towards each other due to the flow-mediated interaction. The lateral force C_L of the two foils is dissimilar from each other, which is different from the almost symmetrical lateral

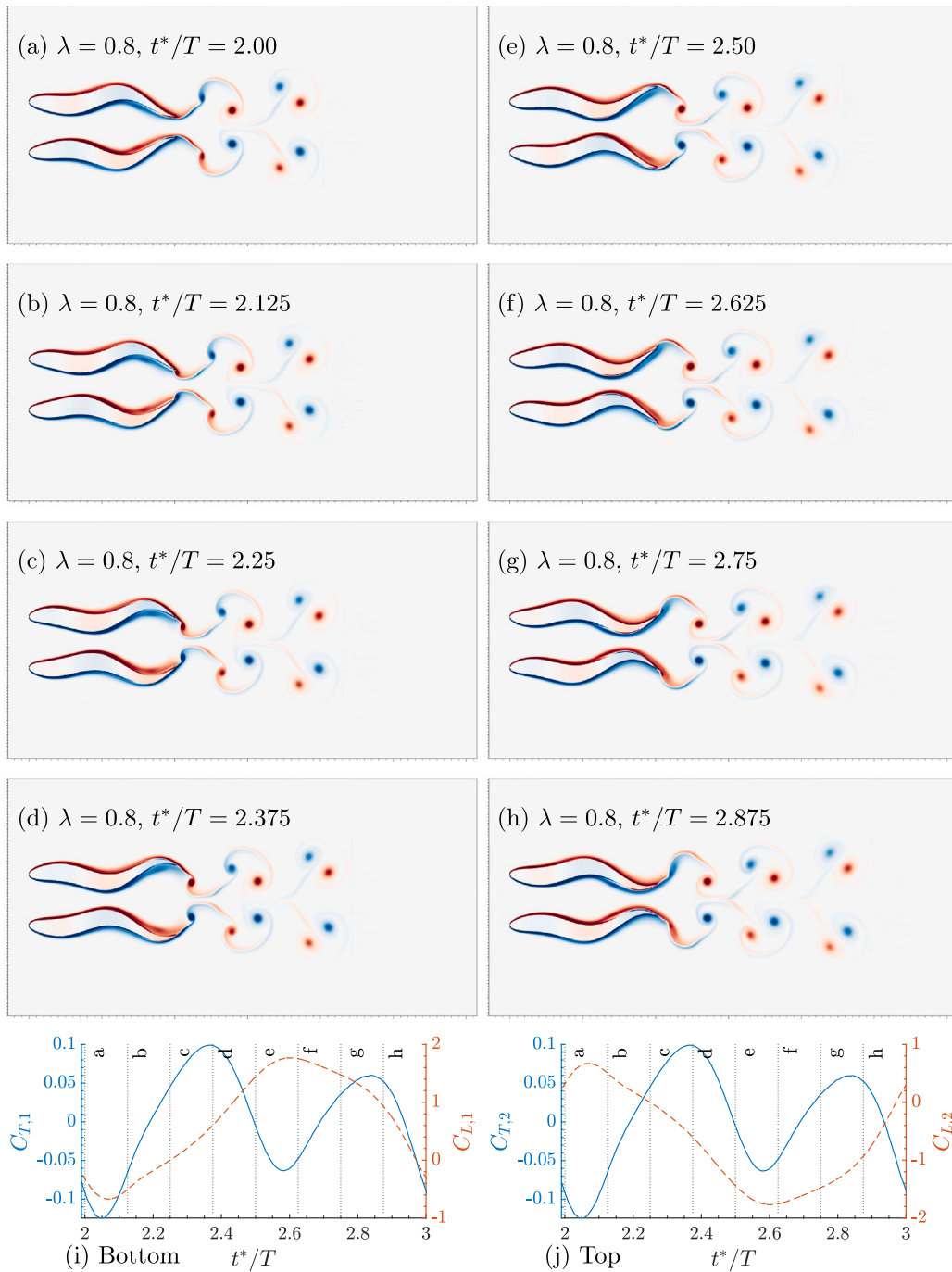


Fig. C.22. Vorticity contours and hydrofoil deformation at Strouhal number $St = 0.4$, wavelength $\lambda = 0.8$, side-by-side arrangement $D = 0$, lateral gap $G = 0.35$, anti-phase $\phi/\pi = 1.0$ at instants of a typical period (a–h) $t^*/T = 2.00 - 2.875$. Time histories of thrust and lift coefficient for the (i) Bottom and (j) Top swimmers. (For interpretation of the references to colour in this figure legend, the reader is referred to the web version of this article.)

force time history at a higher wavelength $\lambda = 2, 8$. In other words, the lateral force is more sensitive to the flow-mediated interaction between the two swimmers. This thrust and lateral force discrepancy may be further relevant to the pressure suction mechanism (Blickhan et al., 1992) that is most typical in low-wavelength swimmers.

At $D = 0.75$, $\lambda = 2$, the leader’s upward vortices collide with the follower’s vortex street, causing a great disturbance in the wake flow of the follower, as seen in Fig. D.26. “Vortex swapping” periodically takes place between the two foils, which is the swapping of positive vortices between the two swimmers: the leader’s positive vortex from previous undulating cycle is entrained by the upward motion the follower’s tail

tip; eventually the leader’s positive vortex pairs up with the follower’s negative one, whereas the follower’s positive vortex moves downward to pair with the leader’s negative one. The thrust C_T of the two swimmers demonstrates a phase difference of about $T/2$, although the lateral force amplitude upon the follower is about 40% larger than that upon the leader. A similar pattern is also observed in the case at $\lambda = 8$, which will be discussed later.

At $D = 0.75$, $\lambda = 8$, the general flow structure is composed of several large vortices, as shown in Fig. D.27, rather than being broken into numerous small ones, as previously seen in Fig. C.24. Periodical interaction occurs in the region between the two foils, whereas in the

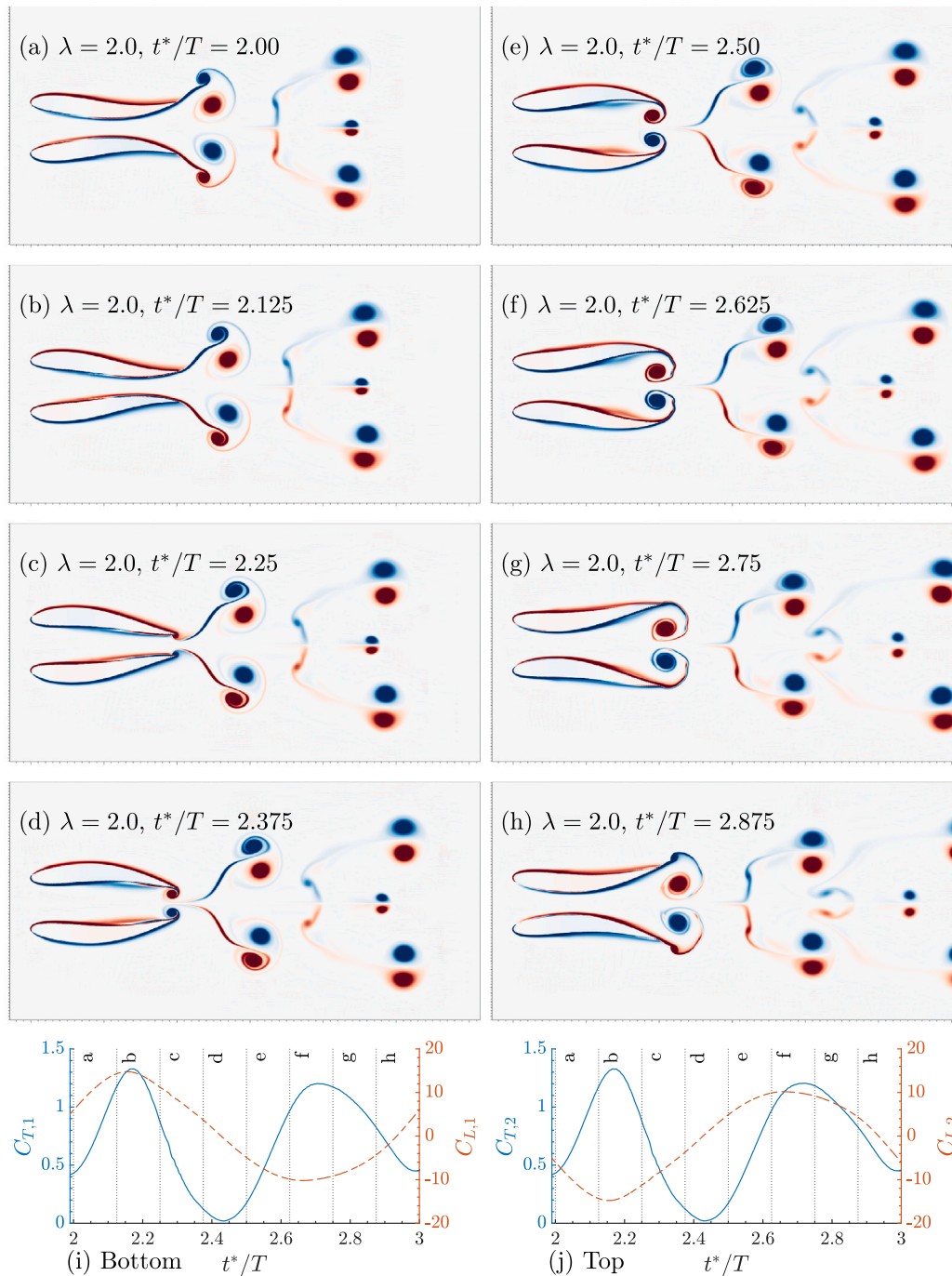


Fig. C.23. Vorticity contours and hydrofoil deformation at Strouhal number $St = 0.4$, wavelength $\lambda = 2.0$, side-by-side arrangement $D = 0$, lateral gap $G = 0.35$, anti-phase $\phi/\pi = 1.0$ at instants of a typical period (a-h) $t^*/T = 2.00 - 2.875$. Time histories of thrust and lift coefficient for the (i) Bottom and (j) Top swimmers. (For interpretation of the references to colour in this figure legend, the reader is referred to the web version of this article.)

wake flow, the vortex interaction is irregular and unpredictable. In the region between the two foils, the vortex pattern near the tail tip of the leader is very similar to that of a single pitching foil (Thekkethil et al., 2018). In contrast, a small vortex is generated from the left side of the follower's head, as seen in Fig. D.27a-h, and then in the next cycle, this small vortex merges with the large vortex produced by the tail pitching of the leader. Despite the irregular wake flow, the merging of small and large vortices is stably repeated in every pitching cycle. In the wake flow region, with the strong disturbance produced by $\lambda = 8$, the front-back distance $D = 0.75$ allows the interaction of vortices generated

from different cycles and swimmers. The vortex dipoles may swap their partners if a collision between the dipoles occurs; the consequent new pair may draw a unique trajectory that further disturbs the wake flow. The thrust and lateral force upon the two foils are generally smooth, as seen in Fig. D.27i and j, corresponding to the relatively stable flow structure near the tail regions of the two foils. The lift force of the two foils are just opposite to each other $C_{L,1} = -C_{L,2}$, i.e. the amplitude of lift force is almost identical, yet the thrust of the follower is generally larger than that of the leader. It is also interesting to note a half-period

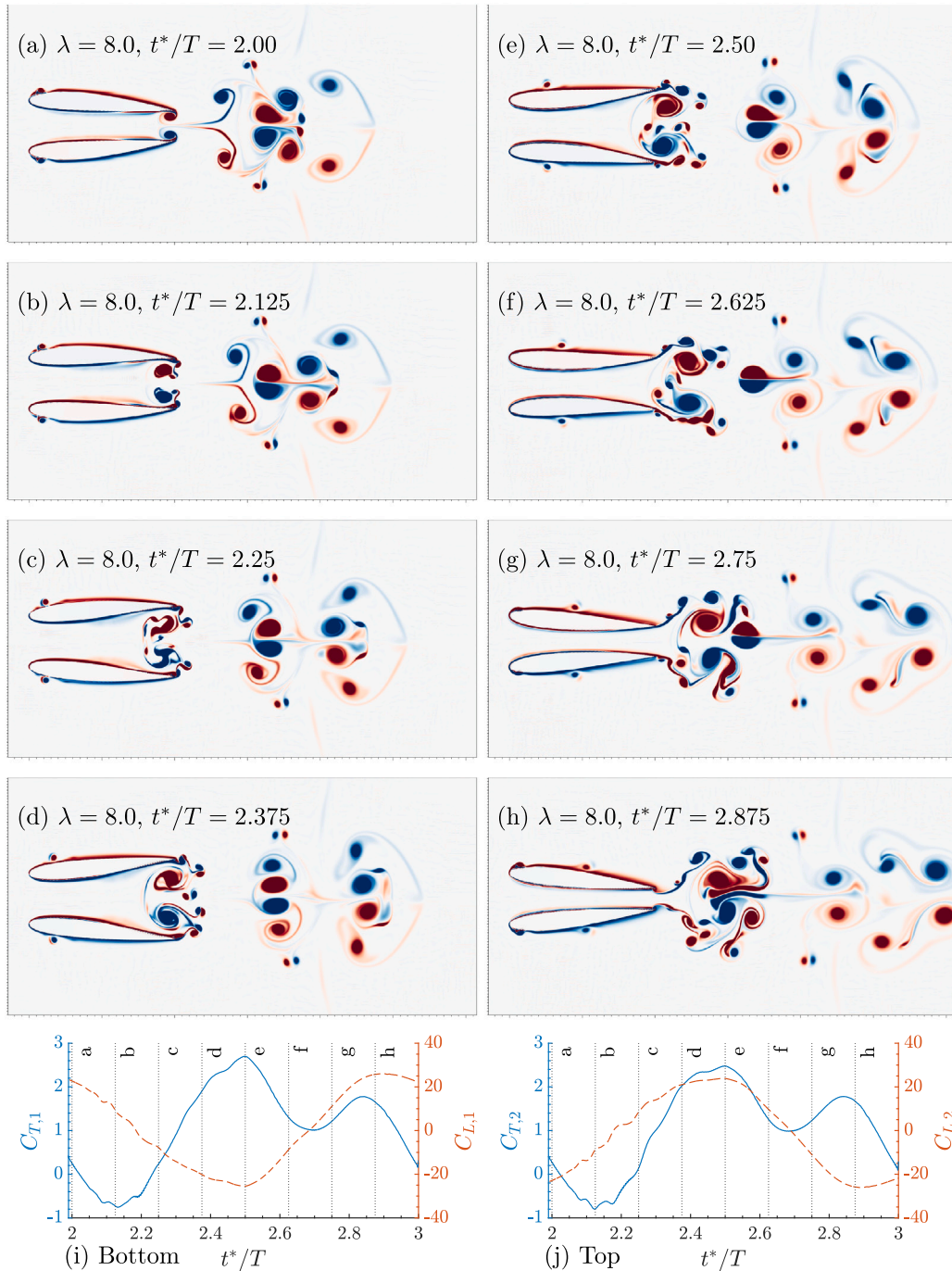


Fig. C.24. Vorticity contours and hydrofoil deformation at Strouhal number $St = 0.4$, wavelength $\lambda = 8.0$, side-by-side arrangement $D = 0$, lateral gap $G = 0.35$, anti-phase $\phi/\pi = 1.0$ at instants of a typical period (a-h) $t^*/T = 2.00 - 2.875$. Time histories of thrust and lift coefficient for the (i) Bottom and (j) Top swimmers. (For interpretation of the references to colour in this figure legend, the reader is referred to the web version of this article.)

phase difference between the leader and the follower’s thrust, which can only be caused by the interaction of the vortex.

Appendix E. Tethered and self-propelling conditions

This section justifies the application of tethered condition to study the accelerating swimmers, although the self-propelling, i.e. free-swimming condition, should be the most accurate representation.

Maertens et al. (2015) reviewed various measures of fish swimming “efficiency”. The “propulsive efficiency” used in the present paper is

equivalent to the “net propulsive efficiency” mentioned in the Maertens et al. (2015), written as $\eta = \frac{C_T}{C_P}$. The optimal “net propulsive efficiency” means the lowest energy consumption to obtain a given acceleration, which differs from the optimal steady swimming efficiency to sustain a certain velocity with zero acceleration. Maertens et al. (2015) proposed a new metric of quasi-propulsive efficiency as $\eta = \frac{C_T + C_D}{C_P}$, adding a separately measured drag term. However, we believe the new metric is more suited for measuring overall swimming performance rather

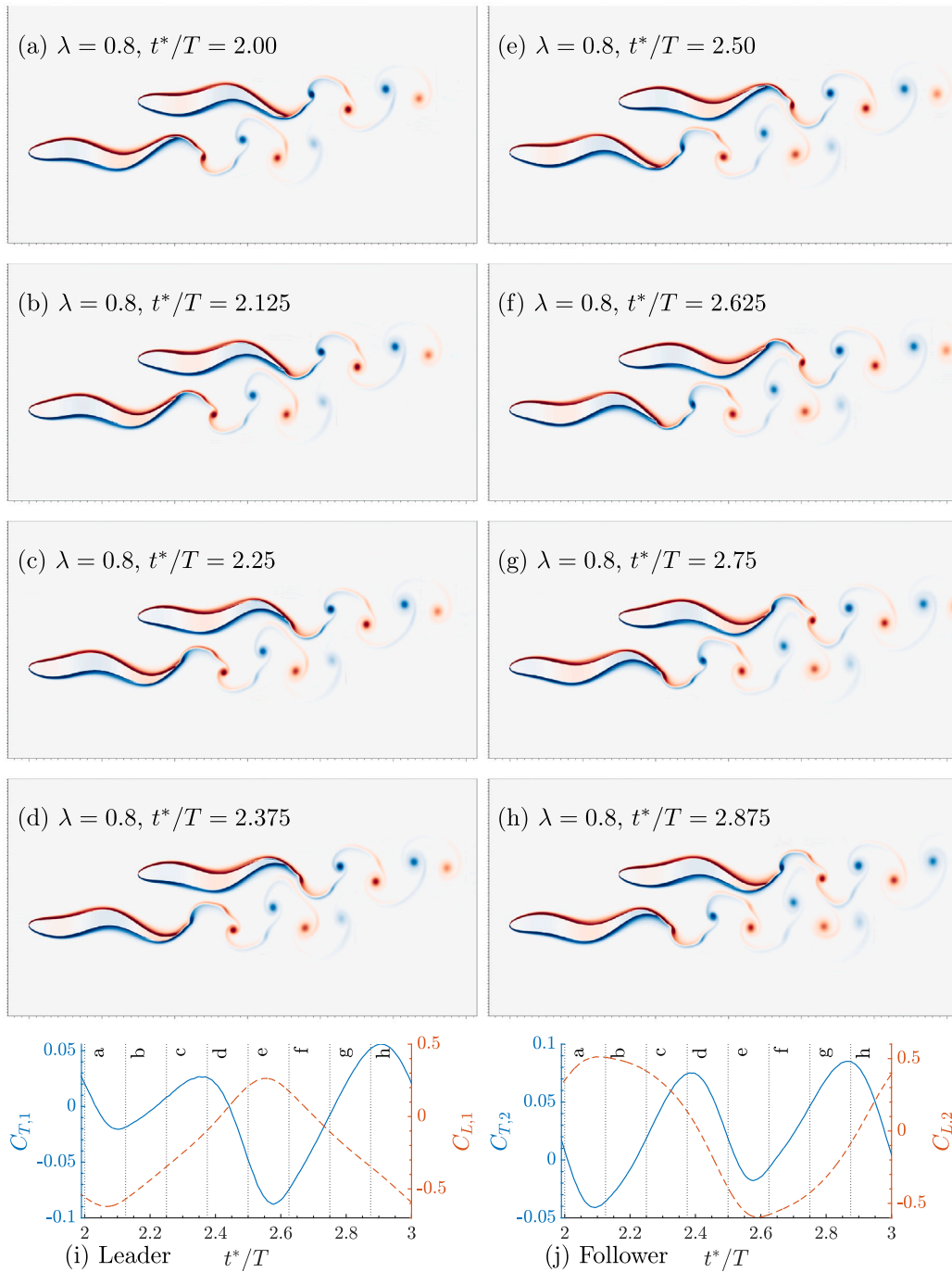


Fig. D.25. Vorticity contours and hydrofoil deformation at Strouhal number $St = 0.4$, wavelength $\lambda = 0.8$, side-by-side arrangement $D = 0.75$, lateral gap $G = 0.35$, anti-phase $\phi/\pi = 1.0$ at instants of a typical period (a-h) $t^*/T = 2.00 - 2.875$. Time histories of thrust and lift coefficient for the (i) Leader and (j) Follower swimmers.

than acceleration performance, which is also discussed in their paper (Maertens et al., 2015). On the other hand, we found that using a tethered/fix setup to investigate thrust generation and acceleration is widely adopted for oscillating/undulating swimmers.

Many studies used the metric of “net propulsive efficiency” with a tethered/fix setup but accelerating/decelerating in a constant free-stream flow, e.g. simulations of two in-line pitching foils (Boschitsch et al., 2014), a wavy foil (Chao et al., 2022), a 3D oscillating wing (Shanmugam and Sohn, 2019), a pitching foil (Alam and Muhammad, 2020), two side-by-side pitching foils (Gungor and Hemmati, 2021), a foil with both heaving and pitching motion (Verma and Hemmati, 2021), a pitching foil with ground effect (Mivehchi et al., 2021) as

well as experiments of flexible pitching foils (Kurt et al., 2021), etc. So utilising the “net propulsive efficiency” should at least be comparable to previous works with the same measure of efficiency.

In addition, Li et al. (2017) proposed a new measure of “Karman gaiting efficiency” for a fish-like swimmer in the altered flow past a half-cylinder; this is an innovative definition, yet it may not be entirely applicable to the present study. Although the hydrofoil swimming in the wake of another one can be similar to “Karman gaiting” by (Li et al., 2017), it cannot account for all the scenarios, especially the side-by-side condition.

In the paper titled “Flow speed has little impact on propulsive characteristics of oscillating foils”, Van Buren et al. (2018) conducted

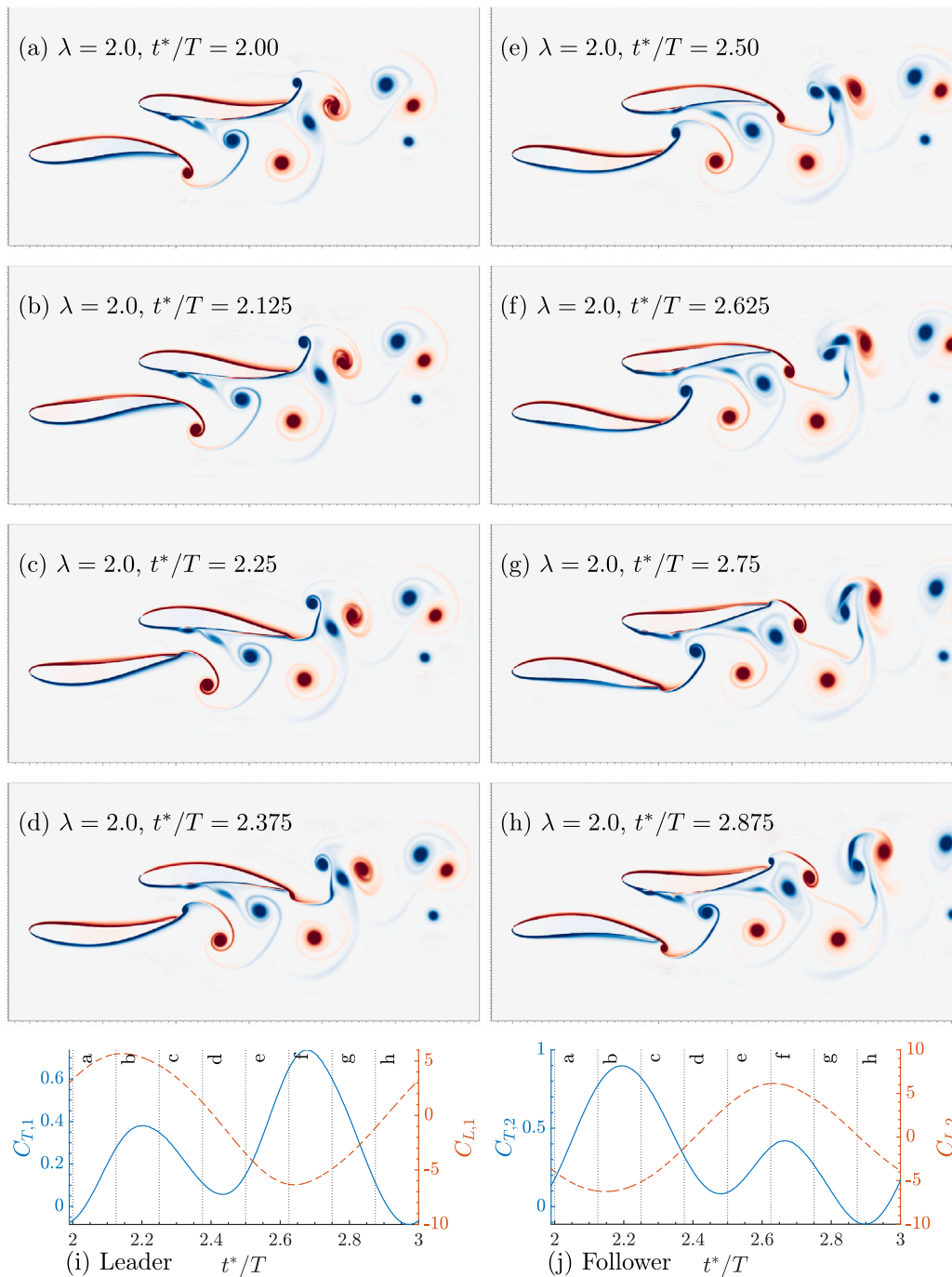


Fig. D.26. Vorticity contours and hydrofoil deformation with wavelength $\lambda = 2.0$, side-by-side arrangement $D = 0.75$, lateral gap $G = 0.35$, anti-phase $\phi/\pi = 1.0$ at instants of a typical period (a-h) $t^*/T = 2.00 - 2.875$. Time histories of thrust and lift coefficient for the (i) Leader and (j) Follower swimmers.

both experimental and theoretical analysis for a heaving and pitching hydrofoil at $4770 < Re < 9550$, whereas the present study fixed Reynolds number at $Re = 5000$. Van Buren et al. (2018) focused on the difference between the tethered and free-swimming configurations including the accelerated condition. They concluded that “constant velocity studies can be used to make robust conclusions about swimming performance without a need to explore the free-swimming condition”. The conclusion by Van Buren et al. (2018) is consistent with slender body theory that flow velocity is not the most important scale for describing the thrust performance but the characteristic velocity of the trailing edge (Smits, 2019). Despite the argument by Van Buren et al. (2018), some researchers still prefer to apply self-propelling rather than

tethered setup, e.g. Paniccia et al. (2021). Yet they did not provide strong counter evidences as well. Some other researchers have gone further to conduct experiments of pitching foils in otherwise still fluids, e.g. Huera-Huarte (2018).

In one of the most recent studies, Zhang et al. (2022) conducted simulation on tethered batoid fish swimming in a constant flow with non-zero net force; they commented that although Van Buren et al. (2018) made valid justification that the performance of the oscillating hydrofoils/fins can be treated identically for tethered and free-swimming conditions, the body drag varies with speed as $\bar{D} \sim \rho s c \bar{U}^2$. For this reason, the total force can still be different between tethered and free-swimming studies.

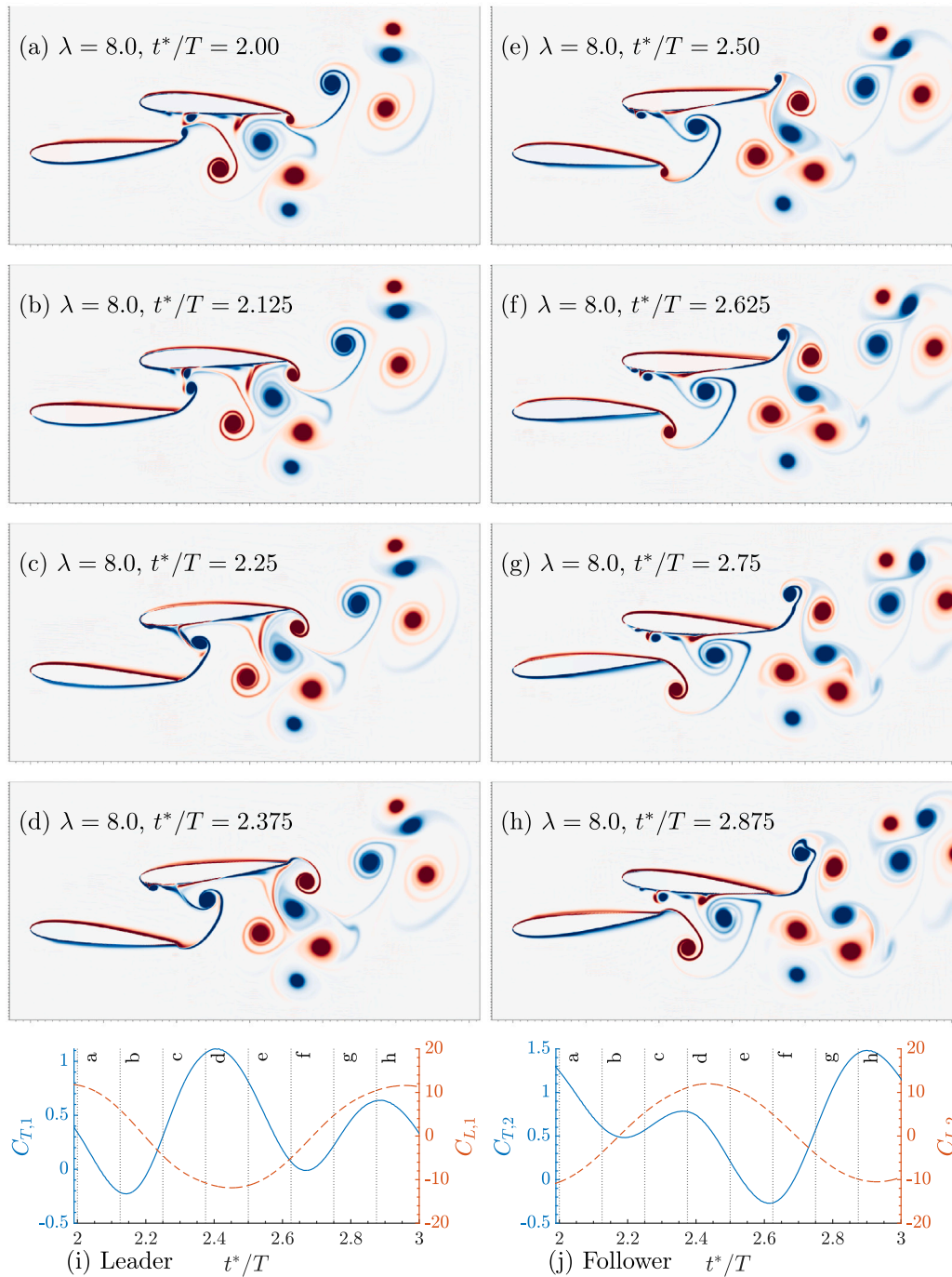


Fig. D.27. Vorticity contours and hydrofoil deformation with wavelength $\lambda = 8.0$, side-by-side arrangement $D = 0.75$, lateral gap $G = 0.35$, anti-phase $\phi/\pi = 1.0$ at instants of a typical period (a-h) $t^*/T = 2.00 - 2.875$. Time histories of thrust and lift coefficient for the (i) Leader and (j) Follower swimmers.

So for the present paper, at long wavelength $\lambda \gg 1$, where the kinematic is very similar to an oscillating foil, the conclusion of Van Buren et al. (2018) can be more applicable, whereas at small wavelength $\lambda \leq 1$, their conclusion can be less applicable, since the kinematic is similar to an anguilliform or carangiform swimmer and the body drag may need to be considered.

In summary, the calculation of “net propulsive efficiency” seems acceptable for the bio-propulsion community as an approximation to the self-propelling/free-swimming condition. However, due to the body drag, the most accurate setup is still the free-swimming conditions.

References

Akanyeti, O., Putney, J., Yanagitsuru, Y.R., Lauder, G.V., Stewart, W.J., Liao, J.C., 2017. Accelerating fishes increase propulsive efficiency by modulating vortex ring geometry. *Proc. Natl. Acad. Sci. USA* 114 (52), <http://dx.doi.org/10.1073/pnas.1705968115>.

Alam, M.M., Muhammad, Z., 2020. Dynamics of flow around a pitching hydrofoil. *J. Fluids Struct.* 99, <http://dx.doi.org/10.1016/j.jfluidstructs.2020.103151>.

Altringham, J.D., Ellerby, D.J., 1999. Fish swimming: Patterns in muscle function. *J. Exp. Biol.* 202 (23), <http://dx.doi.org/10.1242/jeb.202.23.3397>.

- Ashraf, I., Bradshaw, H., Ha, T.T., Halloy, J., Godoy-Diana, R., Thiria, B., 2017. Simple phalanx pattern leads to energy saving in cohesive fish schooling. *Proc. Natl. Acad. Sci. USA* 114 (36), <http://dx.doi.org/10.1073/pnas.1706503114>.
- Ashraf, I., Godoy-Diana, R., Halloy, J., Collignon, B., Thiria, B., 2016. Synchronization and collective swimming patterns in fish (*Hemigrammus bleheri*). *J. R. Soc. Interface* 13 (123), <http://dx.doi.org/10.1098/rsif.2016.0734>.
- Axelsson, B.E., Anker-Nilssen, T., Fossum, P., Kvamme, C., Nøttestad, L., 2001. Pretty patterns but a simple strategy: Predator-prey interactions between juvenile herring and Atlantic puffins observed with multibeam sonar. *Can. J. Zool.* 79 (9), <http://dx.doi.org/10.1139/z01-113>.
- Balay, S., Abhyankar, S., Adams, M.F., Brown, J., Brune, P., Buschelman, K., Dalcin, L., Eijkhout, V., Gropp, W.D., Kaushik, D., et al., 2001. PETSc web page.
- Balay, S., Buschelman, K., Eijkhout, V., Gropp, W., Kaushik, D., Knepley, M., McInnes, L.C., Smith, B., Zhang, H., 2010. PETSc users manual. *ReVision 2* (March).
- Balay, S., Gropp, W.D., McInnes, L.C., Smith, B.F., 1997. Efficient management of parallelism in object-oriented numerical software libraries. In: *Modern Software Tools for Scientific Computing*. http://dx.doi.org/10.1007/978-1-4612-1986-6_8.
- Bhalla, A.P.S., Bale, R., Griffith, B.E., Patankar, N.A., 2013. A unified mathematical framework and an adaptive numerical method for fluid-structure interaction with rigid, deforming, and elastic bodies. *J. Comput. Phys.* 250, <http://dx.doi.org/10.1016/j.jcp.2013.04.033>.
- Bhushan, B., 2009. Biomimetics: Lessons from Nature - an overview. *Phil. Trans. R. Soc. A* 367 (1893), <http://dx.doi.org/10.1098/rsta.2009.0011>.
- Blickhan, R., Krick, C., Zehren, D., Nachtigall, W., Breithaupt, T., 1992. Generation of a vortex chain in the wake of a Suhundulatory swimmer. *Naturwissenschaften* 79 (5), <http://dx.doi.org/10.1007/BF01227131>.
- Borazjani, I., 2013. The functional role of caudal and anal/dorsal fins during the C-start of a bluegill sunfish. *J. Exp. Biol.* 216 (9), <http://dx.doi.org/10.1242/jeb.079434>.
- Borazjani, I., Sotiropoulos, F., 2008. Numerical investigation of the hydrodynamics of carangiform swimming in the transitional and inertial flow regimes. *J. Exp. Biol.* 211 (10), <http://dx.doi.org/10.1242/jeb.015644>.
- Borazjani, I., Sotiropoulos, F., 2009. Numerical investigation of the hydrodynamics of anguilliform swimming in the transitional and inertial flow regimes. *J. Exp. Biol.* 212 (4), <http://dx.doi.org/10.1242/jeb.025007>.
- Borazjani, I., Sotiropoulos, F., 2010. On the role of form and kinematics on the hydrodynamics of self-propelled body/caudal fin swimming. *J. Exp. Biol.* 213 (1), <http://dx.doi.org/10.1242/jeb.030932>.
- Borazjani, I., Sotiropoulos, F., Tytell, E.D., Lauder, G.V., 2012. Hydrodynamics of the bluegill sunfish C-start escape response: Three-dimensional simulations and comparison with experimental data. *J. Exp. Biol.* 215 (4), <http://dx.doi.org/10.1242/jeb.063016>.
- Boschitsch, B.M., Dewey, P.A., Smits, A.J., 2014. Propulsive performance of unsteady tandem hydrofoils in an in-line configuration. *Phys. Fluids* 26 (5), <http://dx.doi.org/10.1063/1.4872308>.
- Burgerhout, E., Tudorache, C., Brittiijn, S.A., Palstra, A.P., Dirks, R.P., van den Thillart, G.E., 2013. Schooling reduces energy consumption in swimming male European eels, *Anguilla anguilla* L. *J. Exp. Mar. Biol. Ecol.* <http://dx.doi.org/10.1016/j.jembe.2013.05.015>.
- Chao, L.-M., Alam, M.M., Cheng, L., 2022. Hydrodynamic performance of slender swimmer: effect of travelling wavelength. *J. Fluid Mech.* 947, A8.
- Cui, Z., Yang, Z., Shen, L., Jiang, H.Z., 2018. Complex modal analysis of the movements of swimming fish propelled by body and/or caudal fin. *Wave Motion* 78, <http://dx.doi.org/10.1016/j.wavemoti.2018.01.001>.
- Daghooghi, M., Borazjani, I., 2015. The hydrodynamic advantages of synchronized swimming in a rectangular pattern. *Bioinspir. Biomim.* 10 (5), <http://dx.doi.org/10.1088/1748-3190/10/5/056018>.
- Dai, L., Wang, X., Staples, K.W., Zhou, C., Tang, H., Xu, L., 2020. Factors influencing successful fishing of tuna free-swimming schools in the equatorial western Pacific ocean. *Turk. J. Fish. Aquat. Sci.* 20 (5), http://dx.doi.org/10.4194/1303-2712-v20_5_02.
- Deng, J., ming Shao, X., 2006. Hydrodynamics in a diamond-shaped fish school. *J. Hydrodyn.* 18 (1), <http://dx.doi.org/10.1007/BF03400483>.
- Dewey, P.A., Quinn, D.B., Boschitsch, B.M., Smits, A.J., 2014. Propulsive performance of unsteady tandem hydrofoils in a side-by-side configuration. *Phys. Fluids* 26 (4), <http://dx.doi.org/10.1063/1.4871024>.
- Dong, G.J., Lu, X.Y., 2007. Characteristics of flow over traveling wavy foils in a side-by-side arrangement. *Phys. Fluids* 19 (5), <http://dx.doi.org/10.1063/1.2736083>.
- Eaton, R.C., Bombardieri, R.A., Meyer, D.L., 1977. The Mauthner-initiated startle response in teleost fish. *J. Exp. Biol.* 66 (1), <http://dx.doi.org/10.1242/jeb.66.1.65>.
- Falgout, R., Cleary, A., Jones, J., Chow, E., Henson, V., Baldwin, C., Brown, P., Vassilevski, P., Yang, U.M., 2010. HYPRE: High performance preconditioners. In: *Users Manual. Version 1*.
- Fish, F.E., 2020. Advantages of aquatic animals as models for bio-inspired drones over present AUV technology. *Bioinspir. Biomim.* 15 (2), <http://dx.doi.org/10.1088/1748-3190/ab5a34>.
- Gazzola, M., Mameau, C., Tchieu, A.A., Koumoutsakos, P., 2012. Flow mediated interactions between two cylinders at finite Re numbers. *Phys. Fluids* 24 (4), 043103. <http://dx.doi.org/10.1063/1.4704195>.
- Godoy-Diana, R., Vacher, J., Raspa, V., Thiria, B., 2019. On the fluid dynamical effects of synchronization in side-by-side swimmers. *Biomimetics* 4 (4), <http://dx.doi.org/10.3390/biomimetics4040077>.
- Griffith, B.E., 2013. IBAMR: An adaptive and distributed-memory parallel implementation of the immersed boundary method. URL <https://ibamr.github.io/about>.
- Griffith, B.E., Patankar, N.A., 2020. Immersed methods for fluid-structure interaction. *Ann. Rev. Fluid Mech.* 52, <http://dx.doi.org/10.1146/annurev-fluid-010719-060228>.
- Guillard, J., Brehmer, P., Colon, M., Guennégan, Y., 2006. Three dimensional characteristics of young-of-year pelagic fish schools in lake. *Aquat. Living Resour.* 19 (2), <http://dx.doi.org/10.1051/alr:2006011>.
- Gungor, A., Hemmati, A., 2020. Wake symmetry impacts the performance of tandem hydrofoils during in-phase and out-of-phase oscillations differently. *Phys. Rev. E* 102 (4), <http://dx.doi.org/10.1103/PhysRevE.102.043104>.
- Gungor, A., Hemmati, A., 2021. The scaling and performance of side-by-side pitching hydrofoils. *J. Fluids Struct.* 104, <http://dx.doi.org/10.1016/j.jfluidstruct.2021.103320>.
- Gupta, S., Thekkethil, N., Agrawal, A., Hourigan, K., Thompson, M.C., Sharma, A., 2021. Body-caudal fin fish-inspired self-propulsion study on burst-and-coast and continuous swimming of a hydrofoil model. *Phys. Fluids* 33 (9), <http://dx.doi.org/10.1063/5.0061417>.
- Hemelrijk, C.K., Hildenbrandt, H., Reinders, J., Stamhuis, E.J., 2010. Emergence of oblong school shape: Models and empirical data of fish. *Ethology* 116 (11), <http://dx.doi.org/10.1111/j.1439-0310.2010.01818.x>.
- Hornung, R.D., Kohn, S.R., 2002. Managing application complexity in the SAMRAI object-oriented framework. *Concurr. Comput.: Pract. Exper.* 14 (5), <http://dx.doi.org/10.1002/cpe.652>.
- Hornung, R.D., Wissink, A.M., Kohn, S.R., 2006. Managing complex data and geometry in parallel structured AMR applications. *Eng. Comput.* 22 (3–4), <http://dx.doi.org/10.1007/s00366-006-0038-6>.
- Huera-Huarte, F.J., 2018. Propulsive performance of a pair of pitching foils in staggered configurations. *J. Fluids Struct.* 81, <http://dx.doi.org/10.1016/j.jfluidstruct.2018.04.024>.
- Hunt von Herbing, I., 2002. Effects of temperature on larval fish swimming performance: The importance of physics to physiology. *J. Fish Biol.* 61 (4), <http://dx.doi.org/10.1006/jfbi.2002.2118>.
- Khalid, M.S.U., Akhtar, I., Dong, H., 2016. Hydrodynamics of a tandem fish school with asynchronous undulation of individuals. *J. Fluids Struct.* 66, <http://dx.doi.org/10.1016/j.jfluidstruct.2016.07.008>.
- Kirk, B.S., Peterson, J.W., Stogner, R.H., Carey, G.F., 2006. libMesh: a C++ library for parallel adaptive mesh refinement/coarsening simulations. *Eng. Comput.* 22 (3–4), <http://dx.doi.org/10.1007/s00366-006-0049-3>.
- Kurt, M., Mivehchi, A., Moored, K., 2021. High-efficiency can be achieved for non-uniformly flexible pitching hydrofoils via tailored collective interactions. *Fluids* 6 (7), <http://dx.doi.org/10.3390/fluids6070233>.
- Kurt, M., Panah, A.E., Moored, K.W., 2020. Flow interactions between low aspect ratio hydrofoils in in-line and staggered arrangements. *Biomimetics* 5 (2), <http://dx.doi.org/10.3390/biomimetics5020013>.
- Lamb, H., 1932. *Hydrodynamics*, sixth ed. Cambridge University Press, Cambridge, p. 182.
- Langley Research Center, 2021. 2DN00: 2D NACA 0012 airfoil validation case. URL https://turbmodels.larc.nasa.gov/naca0012_val.html.
- Lecheval, V., Jiang, L., Tichit, P., Sire, C., Hemelrijk, C.K., Theraulaz, G., 2018. Social conformity and propagation of information in collective u-turns of fish schools. *Proc. R. Soc. B: Biol. Sci.* 285 (1877), <http://dx.doi.org/10.1098/rspb.2018.0251>.
- Li, G., Kolomenskiy, D., Liu, H., Thiria, B., Godoy-Diana, R., 2019. On the energetics and stability of a minimal fish school. *PLoS ONE* <http://dx.doi.org/10.1371/journal.pone.0215265>.
- Li, L., Nagy, M., Graving, J.M., Bak-Coleman, J., Xie, G., Couzin, I.D., 2020. Vortex phase matching as a strategy for schooling in robots and in fish. *Nature Commun.* <http://dx.doi.org/10.1038/s41467-020-19086-0>.
- Li, L., Ravi, S., Xie, G., Couzin, I.D., 2021. Using a robotic platform to study the influence of relative tailbeat phase on the energetic costs of side-by-side swimming in fish. *Proc. R. Soc. A: Math. Phys. Eng. Sci.* 477 (2249), <http://dx.doi.org/10.1098/rspa.2020.0810>.
- Li, C., Yang, W., Xu, X., Wang, J., Wang, M., Xu, L., 2017. Numerical investigation of fish exploiting vortices based on the Kármán gaiting model. *Ocean Eng.* 140, <http://dx.doi.org/10.1016/j.oceaneng.2017.05.011>.
- Liao, J.C., 2007. A review of fish swimming mechanics and behaviour in altered flows. *Philos. Trans. R. Soc. B: Biol. Sci.* 362 (1487), <http://dx.doi.org/10.1098/rstb.2007.2082>.
- Lin, Z., Liang, D., Zhao, M., 2018a. Effects of damping on flow-mediated interaction between two cylinders. *J. Fluids Eng. - ASME* <http://dx.doi.org/10.1115/1.4039712>.
- Lin, Z., Liang, D., Zhao, M., 2018b. Flow-mediated interaction between a vibrating cylinder and an elastically-mounted cylinder. *Ocean Eng.* <http://dx.doi.org/10.1016/j.oceaneng.2018.04.019>.
- Lin, Z., Liang, D., Zhao, M., 2019. Effects of Reynolds number on flow-mediated interaction between two cylinders. *J. Eng. Mech. - ASCE* 145 (12), [http://dx.doi.org/10.1061/\(ASCE\)EM.1943-7889.0001670](http://dx.doi.org/10.1061/(ASCE)EM.1943-7889.0001670).

- Lindsey, C.C., 1978. Form, function, and locomotory habits in fish. *Fish Physiol.* 7 (C), [http://dx.doi.org/10.1016/S1546-5098\(08\)60163-6](http://dx.doi.org/10.1016/S1546-5098(08)60163-6).
- Liu, G., Ren, Y., Dong, H., Akanyeti, O., Liao, J.C., Lauder, G.V., 2017. Computational analysis of vortex dynamics and performance enhancement due to body-fin and fin-fin interactions in fish-like locomotion. *J. Fluid Mech.* 829, <http://dx.doi.org/10.1017/jfm.2017.533>.
- Liu, H., Wassersug, R.J., Kawachi, K., 1996. A computational fluid dynamics study of tadpole swimming. *J. Exp. Biol.* 199 (6), <http://dx.doi.org/10.1242/jeb.199.6.1245>.
- Maertens, A.P., Triantafyllou, M.S., Yue, D.K., 2015. Efficiency of fish propulsion. *Bioinspir. Biomim.* 10 (4), <http://dx.doi.org/10.1088/1748-3190/10/4/046013>.
- Mitsunaga, Y., Endo, C., Babaran, R.P., 2013. Schooling behavior of juvenile yellowfin tuna *Thunnus albacares* around a fish aggregating device (FAD) in the Philippines. *Aquat. Living Resour.* 26 (1), <http://dx.doi.org/10.1051/alr/2012031>.
- Mivehchi, A., Zhong, Q., Kurt, M., Quinn, D.B., Moored, K.W., 2021. Scaling laws for the propulsive performance of a purely pitching foil in ground effect. *J. Fluid Mech.* 919, <http://dx.doi.org/10.1017/jfm.2021.361>.
- Müller, U.K., Smit, J., Stamhuis, E.J., Videler, J.J., 2001. How the body contributes to the wake in undulatory fish swimming: Flow fields of a swimming eel (*Anguilla anguilla*). *J. Exp. Biol.* 204 (16).
- Müller, U.K., Van Den Heuvel, B.L., Stamhuis, E.J., Videler, J.J., 1997. Fish foot prints: Morphology and energetics of the wake behind a continuously swimming mullet (*Chelon labrosus risso*). *J. Exp. Biol.* 200 (22), <http://dx.doi.org/10.1242/jeb.200.22.2893>.
- Nair, S., Kanso, E., 2007. Hydrodynamically coupled rigid bodies. *J. Fluid Mech.* 592, 393–411. <http://dx.doi.org/10.1017/S002211200700849X>, URL <http://www.journals.cambridge.org/abstract/S002211200700849X>.
- Nangia, N., Johansen, H., Patankar, N.A., Bhalla, A.P.S., 2017. A moving control volume approach to computing hydrodynamic forces and torques on immersed bodies. *J. Comput. Phys.* 347, <http://dx.doi.org/10.1016/j.jcp.2017.06.047>.
- Nangia, N., Patankar, N.A., Bhalla, A.P.S., 2019. A DLM immersed boundary method based wave-structure interaction solver for high density ratio multiphase flows. *J. Comput. Phys.* 398, <http://dx.doi.org/10.1016/j.jcp.2019.07.004>.
- Nauen, J.C., Lauder, G.V., 2002. Hydrodynamics of caudal fin locomotion by chub mackerel, *Scomber japonicus* (Scombridae). *J. Exp. Biol.* 205 (12), <http://dx.doi.org/10.1242/jeb.205.12.1709>.
- Paniccia, D., Padovani, L., Graziani, G., Piva, R., 2021. The performance of a flapping foil for a self-propelled fishlike body. *Sci. Rep.* 11 (1), <http://dx.doi.org/10.1038/s41598-021-01730-4>.
- Partridge, B.L., 1981. Internal dynamics and the interrelations of fish in schools. *J. Comp. Physiol. A* 144 (3), <http://dx.doi.org/10.1007/BF00612563>.
- Partridge, B.L., 1982. The structure and function of fish schools. *Sci. Am.* 246 (6), <http://dx.doi.org/10.1038/scientificamerican0682-114>.
- Sfakiotakis, M., Lane, D.M., Davies, J.B.C., 1999. Review of fish swimming modes for aquatic locomotion. *IEEE J. Ocean. Eng.* 24 (2), <http://dx.doi.org/10.1109/48.757275>.
- Shanmugam, A.R., Sohn, C.H., 2019. Numerical investigation on thrust production and unsteady mechanisms of three-dimensional oscillating wing. *J. Mech. Sci. Technol.* 33 (12), <http://dx.doi.org/10.1007/s12206-019-1134-z>.
- Shao, X., Pan, D., Deng, J., Yu, Z., 2010. Hydrodynamic performance of a fishlike undulating foil in the wake of a cylinder. *Phys. Fluids* 22 (11), <http://dx.doi.org/10.1063/1.3504651>.
- Shaw, E., 1978. Schooling fishes. *Am. Sci.* 66 (2).
- Smits, A.J., 2019. Undulatory and oscillatory swimming. *J. Fluid Mech.* <http://dx.doi.org/10.1017/jfm.2019.284>.
- Sui, Y., Chew, Y.T., Roy, P., Low, H.T., 2007. A hybrid immersed-boundary and multi-block lattice Boltzmann method for simulating fluid and moving-boundaries interactions. *Internat. J. Numer. Methods Fluids* 53 (11), <http://dx.doi.org/10.1002/flid.1381>.
- Thekkethil, N., Sharma, A., Agrawal, A., 2018. Unified hydrodynamics study for various types of fishes-like undulating rigid hydrofoil in a free stream flow. *Phys. Fluids* 30 (7), <http://dx.doi.org/10.1063/1.5041358>.
- Thekkethil, N., Sharma, A., Agrawal, A., 2020. Self-propulsion of fishes-like undulating hydrofoil: A unified kinematics based unsteady hydrodynamics study. *J. Fluids Struct.* 93, <http://dx.doi.org/10.1016/j.jfluidstructs.2020.102875>.
- Thekkethil, N., Shrivastava, M., Agrawal, A., Sharma, A., 2017. Effect of wavelength of fish-like undulation of a hydrofoil in a free-stream flow. *Sadhana - Acad. Proc. Eng. Sci.* 42 (4), <http://dx.doi.org/10.1007/s12046-017-0619-7>.
- Trevorrow, M.V., 1998. Salmon and herring school detection in shallow waters using sidescan sonars. *Fish. Res.* 35 (1–2), [http://dx.doi.org/10.1016/S0165-7836\(98\)00054-X](http://dx.doi.org/10.1016/S0165-7836(98)00054-X).
- Triantafyllou, M.S., Triantafyllou, G.S., Yue, D.K., 2000. Hydrodynamics of fishlike swimming. *Annu. Rev. Fluid Mech.* 32, <http://dx.doi.org/10.1146/annurev.fluid.32.1.33>.
- Tytell, E.D., 2004. Kinematics and hydrodynamics of linear acceleration in eels, *Anguilla rostrata*. *Proc. R. Soc. B: Biol. Sci.* 271 (1557), <http://dx.doi.org/10.1098/rspb.2004.2901>.
- Tytell, E.D., Borazjani, I., Sotiropoulos, F., Baker, T.V., Anderson, E.J., Lauder, G.V., 2010. Disentangling the functional roles of morphology and motion in the swimming of fish. *Integr. Comp. Biol.* 50 (6), <http://dx.doi.org/10.1093/icb/icq057>.
- Tytell, E.D., Lauder, G.V., 2004a. The hydrodynamics of eel swimming. *J. Exp. Biol.* 207 (11), <http://dx.doi.org/10.1242/jeb.00968>.
- Tytell, E.D., Lauder, G.V., 2004b. The hydrodynamics of eel swimming: I. Wake structure. *J. Exp. Biol.* 207 (11), <http://dx.doi.org/10.1242/jeb.00968>.
- Tytell, E.D., Lauder, G.V., 2008. Hydrodynamics of the escape response in bluegill sunfish, *Lepomis macrochirus*. *J. Exp. Biol.* 211 (21), <http://dx.doi.org/10.1242/jeb.020917>.
- Uranga, J., Arrizabalaga, H., Boyra, G., Hernandez, C., Goñi, N., 2019. Counting and sizing Atlantic bluefin tuna schools using medium range sonars of baitboats in the Bay of Biscay. *Cont. Shelf Res.* 182, <http://dx.doi.org/10.1016/j.csr.2019.05.013>.
- Van Buren, T., Floryan, D., Wei, N., Smits, A.J., 2018. Flow speed has little impact on propulsive characteristics of oscillating foils. *Phys. Rev. Fluids* 3 (1), <http://dx.doi.org/10.1103/PhysRevFluids.3.013103>.
- Verma, S., Hemmati, A., 2021. Evolution of wake structures behind oscillating hydrofoils with combined heaving and pitching motion. *J. Fluid Mech.* 927, <http://dx.doi.org/10.1017/jfm.2021.750>.
- Videler, J.J., 1993. *Fish Swimming*, Vol. 10. Springer Science & Business Media.
- Videler, J.J., Hess, F., 1984. Fast continuous swimming of two pelagic predators, saithe (*Pollachius virens*) and mackerel (*Scomber scombrus*): a kinematic analysis. *J. Exp. Biol.* 109 (1), 209–228. <http://dx.doi.org/10.1242/jeb.109.1.209>.
- Webb, P.W., 1983. Speed, acceleration and manoeuvrability of two teleost fishes. *J. Exp. Biol.* 102 (1), <http://dx.doi.org/10.1242/jeb.102.1.115>.
- Webb, P.W., 1984. Form and function in fish swimming. *Sci. Am.* 251 (1), <http://dx.doi.org/10.1038/scientificamerican0784-72>.
- Weihls, D., 1973. Hydromechanics of fish schooling. *Nature* 241 (5387), 290–291.
- Weihls, D., 1975. Some hydrodynamical aspects of fish schooling. In: *Swimming and Flying in Nature*. http://dx.doi.org/10.1007/978-1-4757-1326-8_16.
- Wen, L., Ren, Z., Di Santo, V., Hu, K., Yuan, T., Wang, T., Lauder, G.V., 2018. Understanding fish linear acceleration using an undulatory biorobotic model with soft fluidic elastomer actuated morphing median fins. *Soft Robot.* 5 (4), <http://dx.doi.org/10.1089/soro.2017.0085>.
- Wise, T.N., Schwalbe, M.A., Tytell, E.D., 2018. Hydrodynamics of linear acceleration in bluegill sunfish, *Lepomis macrochirus*. *J. Exp. Biol.* 221 (23), <http://dx.doi.org/10.1242/jeb.190892>.
- Zhang, D., Huang, Q.G., Pan, G., Yang, L.M., Huang, W.X., 2022. Vortex dynamics and hydrodynamic performance enhancement mechanism in batoid fish oscillatory swimming. *J. Fluid Mech.* 930, <http://dx.doi.org/10.1017/jfm.2021.917>.
- Zheng, M., Kashimori, Y., Hoshino, O., Fujita, K., Kambara, T., 2005. Behavior pattern (innate action) of individuals in fish schools generating efficient collective evasion from predation. *J. Theoret. Biol.* 235 (2), <http://dx.doi.org/10.1016/j.jtbi.2004.12.025>.